

Determination of the Youngest Active Domain in Major Fault Zones Using Medical X-ray Computed Tomography-derived Density Estimations

akiyuki iwamori (✉ iwamori.akiyuki@d5.kepco.co.jp)

School of Creative Science and Engineering, Waseda University <https://orcid.org/0000-0001-8312-9720>

Hideo Takagi

Faculty of Education and Integrated Arts and Sciences, Waseda University

Nobutaka Asahi

Dia Consultants Co. Ltd.

Tatsuji Sugimori

Dia Consultants Co. Ltd.

Eiji Nakata

Central Research Institute of Electric Power Industry

Shintaro Nohara

Central Research Institute of Electric Power Industry

Keiichi Ueta

Central Research Institute of Electric Power Industry

Research Article

Keywords: medical X-ray CT, CT number, beam hardening, bulk density, effective atomic number, rock/protolith density ratio, the youngest active domain of a fault zone

Posted Date: April 1st, 2021

DOI: <https://doi.org/10.21203/rs.3.rs-342540/v1>

License:   This work is licensed under a Creative Commons Attribution 4.0 International License.

[Read Full License](#)

1 **Determination of the youngest active domain in major fault**
2 **zones using medical X-ray computed tomography-derived**
3 **density estimations**

4 Akiyuki Iwamori^{1,2}

5 Corresponding author

6 Email: iwamori.akiyuki@d5.kepco.co.jp

7

8 Hideo Takagi³

9 Email: hideo@waseda.jp

10

11 Nobutaka Asahi⁴

12 Email: n.asahi@diaconsult.co.jp

13

14 Tatsuji Sugimori⁴

15 Email: T.Sugimori@diaconsult.co.jp

16

17 Eiji Nakata⁵

18 Email: nakata@criepi.denken.or.jp

19

20 Shintaro Nohara⁵

21 Email: nohara-s@criepi.denken.or.jp

22

23 Keiichi Ueta⁵

24 Email: ueta@criepi.denken.or.jp

25

26 (Institutional addresses)

27 ¹ Kansai Electric Power Co. Inc., 3-6-16, Nakanosihma, Kita-ku, Osaka, 530-8270, Japan

28 ² School of Creative Science and Engineering, Waseda University, 1-6-1, Nishiwaseda,

29 Shinjuku-ku, Tokyo, 169-8050, Japan

30 ³ Faculty of Education and Integrated Arts and Sciences, Waseda University, 1-6-1,

31 Nishiwaseda, Shinjuku-ku, Tokyo, 169-8050, Japan

32 ⁴ Dia Consultants Co. Ltd., 5-3, Toyotsu-cho, Suita-shi, Osaka, 564-0051, Japan

33 ⁵ Central Research Institute of Electric Power Industry, 1646 Abiko, Abiko-shi, Chiba, 270-

34 1194, Japan

35

36 **Abstract**

37 Determination of the youngest active domains in fault zones that are not overlain by Quaternary

38 sedimentary cover are critical for evaluating recent fault activity, determining the current local
39 stress field, and mitigating the impacts of future earthquakes. Considering the exhumation of a
40 fault zone, the youngest active domain in a fault zone is supposed to correspond to the activity
41 at the minimum fault depth of a buried fault, such that the most vulnerable area, which possesses
42 the lowest rock/protolith density ratio, is assumed to be indicative of this recent fault activity.
43 However, it is difficult to measure the density of fault rocks and map the rock/protolith density
44 ratio across a given fault zone. Here we utilize medical X-ray computed tomography (CT), a
45 non-destructive technique for observing and analyzing materials, to investigate the fault
46 characteristics of several fault zones and their surrounding regions in Japan, and attempt to
47 determine the youngest active domain of a given fault zone based on its CT numbers, which are
48 a function of the density and effective atomic number of the fault rock and protolith. We first
49 investigate the density, void ratio, and effective atomic number of active and inactive fault rocks,
50 and their respective protoliths. We then calculate the CT numbers after reducing the beam-
51 hardening effects on the rock samples, and study the relationships among the CT number,
52 density, and effective atomic number. We demonstrate that the density, effective atomic number,
53 and CT number of the fault rock decrease as the youngest active zone is approached, such that
54 the region with the lowest CT number and rock/protolith density ratio defines the youngest
55 active domain of a given fault zone.

56

57 **Keywords**

58 medical X-ray CT, CT number, beam hardening, bulk density, effective atomic number,
59 rock/protolith density ratio, the youngest active domain of a fault zone

60

61 **1 Introduction**

62 Determination of the youngest active domain in fault zones that are not overlain by Quaternary
63 cover are integral not only for evaluating fault activity and restoring the most recent stress field
64 using slip data, but also for proposing local/regional earthquake disaster mitigation measures.
65 Various methods have been employed to potentially determine the youngest active domain in
66 fault zones in bedrock (e.g., Mizoguchi and Ueta, 2012; Shigematsu et al., 2017; Tanaka et al.,
67 2018). Considering the exhumation of a fault zone, this youngest active domain in a fault zone
68 is supposed to correspond to the activity at the minimum fault depth of a buried fault, such that
69 this most vulnerable area is assumed to be the area that possesses the lowest rock/protolith
70 density ratio. Previous studies have focused on the density of the rocks around the fault zone
71 (e.g., Morrow and Lockner, 2001; Takeuchi et al., 2005); however, a quantitative density-based
72 classification of fault rocks has not been performed to date. Ikeda et al. (2001) performed
73 geophysical well logging in the borehole through the Nojima Fault Zone, which was active

74 during the 1995 Hyogo-ken Nanbu Earthquake, and reported that the non-fractured granite and
75 the fault zone densities were 2.6–2.7 and 1.5–2.5 g/cm³, respectively. However, it is difficult to
76 measure the density of fault rocks. Here we utilize medical X-ray computed tomography (CT)
77 in an attempt to determine the youngest active domain in a given fault zone based on its CT
78 numbers.

79 X-ray CT is a non-destructive technique that images the three-dimensional (3D) internal
80 structure of materials. The potential of X-ray CT in geoscience was recognized soon after its
81 development as a medical imaging technique in 1972 (Hounsfield, 1973), resulting in numerous
82 geoscience applications since the 1980s (e.g., Wellington and Vinegar, 1987; Raynaud et al.,
83 1989; Orsi et al., 1994; Boespflug et al., 1995; Verhelst et al., 1996; Geet et al., 2000; Ueta et
84 al., 2000). Hirono et al. (2008) used X-ray CT to analyze the fault rocks generated during the
85 1999 Chi-Chi Earthquake; however, they were unable to report on the relationship between the
86 CT number and fault rock density, owing to the beam hardening (BH) effect. Aiyama et al.
87 (2017) recently observed the internal structure of a fault fracture zone using medical X-ray CT,
88 and reported that the CT image of the fault gouge zone was darker and less dense than that of
89 the surrounding cataclasite.

90 X-ray CT is generally conducted using either industrial- or medical-grade scanners. Industrial
91 scanners employ high-energy X-rays, and are used to examine dense rocks or minerals. Medical

92 scanners can also be employed in a geoscience context to study low-density, unconsolidated
93 sediments (Nishizawa et al., 1995). Medical scanners are easier to operate than industrial
94 scanners, but the resulting CT images, which are obtained at lower X-ray intensities, include
95 artifacts, such as BH (Ketchman and Carlson, 2001). Nakano et al. (2000) observed and
96 analyzed the internal structures of lake sediment, basalt, and granite samples using a medical
97 scanner after accounting for X-ray attenuation and reducing the BH effect. However, the
98 applicability of their methodology is not straightforward because a priori knowledge of the X-
99 ray spectrum of the scanner is required. Ketchman and Hanna (2014) and Geet et al. (2000)
100 investigated the use of micro-CT in reducing the BH effects. Geet et al. (2000) estimated the
101 density and effective atomic number via the dual-energy method, which uses CT images
102 acquired at two different tube voltages; this approach is used to discriminate materials by
103 focusing on changes in the contrast of the CT images due to the X-ray energy differences of the
104 imaged materials.

105 Iwamori et al. (2020) investigated six different mineral samples with known densities and
106 effective atomic numbers using medical CT images, and defined the CT values for these
107 minerals, thereby providing an effective way to reduce the BH effect. Iwamori et al. (2020) also
108 presented a method for determining the density and effective atomic number via the dual-energy
109 method, and a method for estimating the density and effective atomic number using CT images

110 taken with one tube voltage.

111 Here we present a method to determine the youngest active domain in major fault zones using
112 medical X-ray CT characteristics on the fault rock densities and effective atomic numbers. We
113 first investigate the density, void ratio, and effective atomic number of active and inactive fault
114 rocks, and their respective protoliths. We then calculate the CT numbers from CT images where
115 the BH effects have been reduced, and study the relationship among the CT number, density,
116 and effective atomic number. We reduce the effects of sample thickness variations and CT
117 image quality deterioration due to the X-ray energy reduction by adjusting the sample size and
118 imaging direction based on a ~10 cm X-ray transmission thickness.

119

120 **2 Geological structural characteristics and rock structural** 121 **properties of each analyzed fault**

122 We analyzed three faults, the Median Tectonic Line (MTL), and the Yamada and Tsuruga faults,
123 for our medical X-ray CT analysis. We chose the MTL since it is one of the longest onshore
124 faults in Japan, with both active and inactive fault outcrops; the protoliths of the fault rocks
125 consist mainly of Sanbagawa schists and Ryoke tonalites. We chose the Yamada Fault as an
126 example of an active fault in granite, and the Tsuruga Fault as an example of an active fault at
127 the geological boundary between metabasalt and granite. We focused on the fault rocks in the

128 basement rock since the fault rock characteristics of the basement rock and basement rock–
129 sediment contact zone are thought to be different. The sample details are provided in Table 1,
130 with the geological outline of the study region and detailed geological maps of the investigated
131 faults shown in Figs 1 and 2, respectively. Here we define an "active fault" as a fault that has
132 been active since the late Pleistocene, and an "inactive fault" as a fault that has no recorded
133 activity since the late Pleistocene.

134 [<Table 1](#) [<Figure 1](#) [<Figure 2](#)

135

136 **2.1 MTL in the Ina area, Nagano Prefecture (Hiji outcrop; active fault)**

137 The MTL is the longest onshore fault and extends across the central part of southwestern Japan
138 for more than 1,000 km (e.g., Okada, 1992). The MTL is an approximately N–S-trending,
139 vertically dipping feature in the Ina area of Nagano Prefecture. Mylonitic rocks that originated
140 from Hiji tonalite are distributed within ~1 km of the western side of the MTL in this area, with
141 increasing grain-size reduction and alteration closer to the MTL; however, fault breccia and
142 fault gouge are scarcely observed (Takagi, 1984). Conversely, the Sanbagawa schist on the
143 eastern side of the MTL is clayey and/or contains fractured lenticular bodies within a few meters
144 of the MTL, with minimal macroscopic fractures 10–20 m from the MTL (Takagi, 1984).

145 The Hiji outcrop (35.80278°N, 138.08278°E) is located under a playground on the eastern bank

146 of Lake Miwa, a dammed reservoir in the Ina area. The MTL, which forms the boundary
147 between the Hiji tonalite and the Sanbagawa schist (Fig. 3a), is clearly exposed, except in spring
148 when the reservoir is full. The fault is located ~80 cm east of the MTL in this outcrop, where it
149 cuts a <100 ka terrace gravel deposit, and extends into the Sanbagawa schist without being
150 displaced by other foliations (Takagi et al., 2019). The strike and dip of the youngest fault plane
151 Y are N3E and 74W, respectively, and the observed striations on the slip plane possess a rake
152 of 20–30N (Fig. 3a). The fault gouge zone along fault plane Y clearly shows a dextral sense of
153 shear (Fig. 3a, b). The observed displacement of 60 cm at the base of the terrace gravel deposit
154 due to fault plane Y equates to a real displacement velocity of 0.012–0.0118 m/ky along this
155 fault, assuming the gravel layer was deposited 100,000 years ago (Takagi et al., 2019).

156 Sample HJ-8, which was derived from the Sanbagawa pelitic schist, was taken from the fault
157 zone that formed during the most recent fault activity at the Hiji outcrop. This fault rock sample
158 (Fig. 3b) can be divided into five zones based on their degree of cohesiveness and the
159 classification of Takagi and Kobayashi (1996). Zones HJ8-2–HJ8-4 are classified as fault
160 gouges, whereas zones HJ8-1 and HJ8-5 are cataclasites; the boundary between zones HJ8-2
161 and HJ8-3 is defined by the main fault plane Y, which cuts the terrace gravel deposit (Fig. 3b).

162 Protolith sample MZ-5 was collected from an outcrop (35.79150°N, 138.08269°E) located ~20
163 m east of the Mizoguchi outcrop (1.2 km south of the Hiji outcrop), which is where the MTL

164 crops out; this sample was selected for comparison with the fault rocks.

165 Photomicrographs of the fault rocks are shown in Fig. 3c, d. The cataclasite zone (HJ8-1)
166 contains mainly ≤ 1 -mm-diameter quartz and albite fragments, with a dextral sense of slip
167 observed. Fine-grained clay minerals are distributed uniformly in the fault gouge zone (HJ8-3),
168 which is adjacent to fault plane Y, with a dextral sense of slip indicated. Sample MZ-5 consists
169 mainly of quartz, albite, phengite, calcite, and chlorite.

170 <Figure 3

171

172 **2.2 MTL in the Matsusaka area, Mie Prefecture (Awano–Tabiki outcrop; inactive**
173 **fault)**

174 The MTL is an approximately E–W-trending feature in the Matsusaka area of Mie Prefecture
175 (Nishioka et al., 2010; Fig. 2b) that does not disrupt lower river terrace deposits, which means
176 that there has been no known activity during the late Quaternary (Okada, 1992). The Hatai
177 tonalite is distributed within 2 km of the northern side of the MTL in this area, and consists
178 mainly of plagioclase, hornblende, and chloritized biotite. The Hatai tonalite is affected by
179 mylonitization along the MTL, and contains foliations that are almost parallel to the MTL
180 (Takagi, 1985).

181 The Awano–Tabiki outcrop (34.44294°N, 136.25292°E) is located in Awano and Tabiki,

182 Matsusaka City, Mie Prefecture. This outcrop comprises Ryoke Hatai tonalite and Sanbagawa
183 schist (Fig. 3e). The Hatai tonalite consists of weathered, light-brown fault rocks with irregular
184 but well-developed cracks, and scarcely observed fault breccia and fault gouge in the Ryoke
185 Belt. Conversely, the Sanbagawa schist is partly clayey and shows a dextral sense of shear
186 within 2 m of the MTL, with minimal macroscopic fractures 10–20 m from the MTL.

187 Shigematsu et al. (2017) reported that four stages of deformation have been recorded in the
188 fault zone at this outcrop since the Paleocene, with the final stage consisting of Miocene-age
189 normal faulting. Here we investigated faults on the boundary between the Ryoke and
190 Sanbagawa belts, with a focus on one of the two faults that Shigematsu et al. (2017) evaluated
191 as possessing the youngest active domain.

192 The fault on the boundary between the Ryoke and Sanbagawa belts shows good continuity
193 throughout the outcrop and is not disrupted by other faults. The most recent fault plane strikes
194 N76E and dips 31N, with the striations on the slip plane possessing a rake of 88NNW. The fault
195 gouge zone (1–3 cm wide) along this fault shows a normal sense of shear, which is consistent
196 with the observed features that Shigematsu et al. (2017) identified as the final stage of
197 deformation (Fig. 3e, f).

198 Sample AT was taken from the fault zone that formed during the most recent fault movement
199 at this outcrop (Fig. 3f). This fault rock sample can be divided into five zones, based on their

200 degree of cohesiveness: AT-2 and AT-3 are fault gouges, and AT-1, AT-4, and AT-5 are
201 cataclasites. AT-1 and AT-2 correspond to the Sanbagawa Belt, and zones AT-3, AT-4, and AT-5
202 correspond to the Ryoke Belt, with the boundary between AT-2 and AT-3 representing the main
203 fault plane (Y) of the geological MTL boundary.

204 We collected four rock samples from the Ryoke Belt (ATR and HA samples) and two rock
205 samples from the Sanbagawa Belt (ATS samples) for analysis. Cataclasite samples ATR-2 and
206 ATR-3 were collected ~5 m to the north of the MTL (Fig. 3e), mylonite sample ATR-4 was
207 collected 300 m to the north of the MTL (Fig. 2b), and protolith sample HA-1 (Fig. 7g) was
208 collected 13.5 km ENE of the outcrop (Fig. 2b) to provide a comparison of the fault rock and
209 protolith characteristics with different degrees of cohesiveness. Protolith samples ATS-1 (20 m
210 to the south of the MTL) and ATS-2 (550 m to the south of the MTL) were collected from the
211 Sanbagawa Belt (Figs 3c and 2b). ATS-2 is a solid pelitic schist with well-developed schistosity,
212 whereas ATS-1 contains 2-cm-diameter quartz crystals. The cataclasite samples from the Hatai
213 tonalite were analyzed using X-ray CT imaging (ATR-2) and density and X-ray fluorescence
214 (XRF) analyses (ATR-3).

215 Photomicrographs of the fault rocks are shown in Fig. 3g, h. The thin AT section can be divided
216 into three zones, AT-1, AT-2, and AT-4, with the youngest fault plane Y extending through the
217 section without being displaced by other foliations. Zone AT-1, which consists of a Sanbagawa

218 cataclasite, mainly contains ≤ 0.2 -mm-diameter albite fragments, and shows a reverse sense of
219 shear. Zone AT-4, which consists of a Ryoke cataclasite, contains ≤ 0.5 -mm-diameter
220 mylonitized quartz fragments that have been affected by cataclastic flow, and 0.2-mm-wide
221 calcite veins that have been displaced by a reverse sense of Riedel shearing. Fine-grained clay
222 minerals are uniformly distributed throughout the fault gouge in zone AT-2, with a normal sense
223 of slip indicated.

224 ATS-2, which is a Sanbagawa schist protolith, consists mainly of fine quartz, albite, phengite,
225 and calcite crystals (≤ 0.2 -mm-diameter crystals), and ATS-1 contains mainly ≤ 0.2 -mm-
226 diameter quartz, albite, phengite, and graphite fragments. ATS-2 contains less phengite than
227 ATS-1, and the schistosity of both samples are regulated by the arrangement of the quartz and
228 albite aggregates and/or phengite.

229 Samples HA-1 and ATR-4 consist mainly of quartz, plagioclase, hornblende, and chlorite. HA-
230 1 contains ≤ 2 -mm-diameter plagioclase and amphibole crystals and ≤ 0.5 -mm-diameter quartz
231 and chlorite crystals. Conversely, the mylonite ATR-4 sample contains ≤ 1 -mm-diameter
232 plagioclase and hornblende crystals, and voids that are filled with recrystallized quartz
233 aggregates. The cataclasite ATR-3 sample consists mainly of ≤ 0.2 -mm-diameter plagioclase,
234 quartz, and chlorite crystals and mylonitized quartz fragments that have been affected by
235 cataclastic flow.

236

237 **2.3 Tsuruga Fault (Oritodani outcrop; active fault)**

238 The Tsuruga Fault is a ~25-km-long, NE–SW-trending, right-lateral strike-slip fault in the
239 central Fukui Prefecture (National Institute of Advanced Industrial Science and Technology,
240 2016). Koujaku granite (Upper Cretaceous) and metabasalt (Middle–Upper Jurassic
241 accretionary complex) from the Mino–Tanba Belt occur around this fault (Fig. 2c). Kurimoto
242 et al. (1999) performed a trench excavation in the Ikenotani area and reported that the southern
243 part of the Tsuruga Fault was active between the latter half of the twelfth and end of the
244 fourteenth centuries, with a vertical displacement of 1.5–2 m and average vertical displacement
245 velocity of 0.5–0.6 m/10³ years.

246 The Oritodani outcrop (35.53750°N, 136.01906°E), which is located 1.7 km southwest of the
247 Ikenotani area, contains exposures of Koujaku granite and metabasalt, with a 10–20-cm-wide
248 fault gouge distributed along the geological boundary (Fig. 4a). The boundary fault between
249 the granite and metabasalt is continuous throughout the outcrop and cuts the terrace gravel
250 deposit. The strike and dip of the most recent fault plane are N49E and 78W, respectively, with
251 the striations on the slip plane possessing a rake of 15N. A very soft fault gouge (T-3-3 zone) is
252 developed in the metabasalt along its boundary with the granite fault gouge (T-3-2 zone) and
253 shows a dextral sense of shear (Fig. 4b, e).

254 Sample T-3 was taken from the fault zone that formed during the most recent fault activity at
255 the Oritodani outcrop. This fault rock sample (Fig. 4b) can be divided into four zones based on
256 their degree of cohesiveness: T-3-1, T-3-2, and T-3-3 are fault gouges, and T-3-4 is a cataclasite.
257 T-3-1 and T-3-2 correspond to the Koujaku granite, and T-3-3 and T-3-4 correspond to the
258 metabasalt, with the main fault plane (Y) of the Tsuruga Fault extending through T-3-3. The
259 brown (T-3-1) and white (T-3-2) fault gouge zones are slightly harder than the T-3-3 zone, with
260 the P foliations in T-3-2 that have developed near the boundary with T-3-1 exhibiting a dextral
261 sense of slip (Fig. 4b), which indicates that the zone up to 10 cm from the main fault plane was
262 possibly affected by the most recent fault activity.

263 We collected cataclasite sample C-2 and protolith sample K-1 from the Koujaku granite at the
264 Oritodani outcrop to compare the degrees of cohesiveness in the samples. We also collected
265 cataclasite sample C-1 and protolith sample T-5 from the metabasalt of the Mino–Tanba Belt.

266 Photomicrographs of the fault rocks are shown in Fig. 4c, d, and e. The youngest fault plane Y
267 extends through T-3-3 without being displaced by other foliations. Fine-grained clay minerals
268 are distributed uniformly throughout fault gouge T-3-3, and developed P foliations with a
269 dextral sense of slip are present. Conversely, fault gouge T-3-2 mainly contains ≤ 0.2 -mm-
270 diameter quartz, K-feldspar, and plagioclase fragments and no clear fault plane (Fig. 4c, d).
271 Therefore, the youngest activity of this fault is thought to have only been recorded in the most

272 vulnerable fault gouge (T-3-3).

273 Protolith sample K-1 mainly consists of ≤ 3 -mm-diameter quartz, plagioclase, K-feldspar and
274 biotite crystals. Cataclasite sample C-2 mainly consists of ≤ 0.3 -mm-diameter quartz,
275 plagioclase, K-feldspar, and biotite crystals. Conversely, sample T-5 mainly consists of ≤ 0.1 -
276 mm-diameter hornblende and clinopyroxene crystals, whereas sample C-1 mainly consists of
277 hornblende, chlorite, and plagioclase fragments, and fewer hornblende crystals than in sample
278 T-5.

279 <Figure 4

280

281 **2.4 Yamada Fault (Musyu outcrop; active fault)**

282 The Yamada Fault Zone is an ENE–WSW-trending dextral fault that forms the ~ 33 -km-long
283 Yamada Fault Zone at the base of the Tango Peninsula, northern Kyoto Prefecture (Earthquake
284 Research Committee, 2004). This fault zone is composed of the Yasukeyama, Yamada, and
285 Koryuji faults; we hereafter identify the Yamada Fault Zone as the Yamada Fault. Miyazu
286 granite (Upper Cretaceous–Paleogene) is present around the Yamada Fault (Fig. 2d).

287 The Mushu outcrop (35.51722°N , 136.00797°E) contains a cataclasite zone of Miyazu granite,
288 and a fault with a 1–2-cm-wide fault gouge that is continuous throughout the outcrop (Fig. 4f).

289 The strike and dip of the youngest fault plane are N55E and 62W, respectively, with striations

290 on the slip plane possessing a rake of 20S. The fault gouge zone is very soft, and shows a dextral
291 sense of shear. Aiyama et al. (2017) investigated the activity of this fault in the Mushu outcrop,
292 and reported that the main fault plane, which has been active during the Quaternary, contains a
293 fault gouge zone. Aiyama et al. (2017) also characterized this fault gouge zone as a layered
294 structure with ten fault gouge layers that are indicative of repetitive activity after smectite
295 crystallization. Iwamori et al. (2015) studied the activity of the Yamada Fault over the last
296 ~200,000 years based on the faults that cut the sedimentary layer above the Mushu outcrop, and
297 reported that the youngest fault activity occurred between 2,000 and 200 years B.P.

298 Sample YDA was taken from the fault zone that formed during the most recent fault activity at
299 the Mushu outcrop (Fig. 4g). This fault rock sample can be divided into four zones based on
300 their degree of cohesiveness: YDA-1 and YDA-2 are fault breccias, YDA-3 is a fault gouge,
301 and YDA-4 is a cataclasite. The boundary between YDA-2 and YDA-3 represents the main
302 fault plane Y, and the fault breccias are dark brown due to iron oxide deposition. We collected
303 a Miyazu granite protolith sample (YK-1) at Karakawa, ~6 km WSW of the Mushu outcrop,
304 for comparison with the fault rocks.

305 Photomicrographs of the fault rocks are shown in Fig. 4h, i. The youngest fault plane Y extends
306 along the boundary between the YDA-2 and YDA-3 fault gouge zones without being displaced
307 by other foliations. YDA-3 consists of a fine-grained clay mineral matrix that contains a mainly

308 uniform distribution of ≤ 0.2 -mm-diameter quartz, K-feldspar, and plagioclase fragments, and
309 possesses a P foliation that indicates a dextral sense of slip. Conversely, fault breccia YDA-2
310 mainly consists of ≤ 0.3 -mm-diameter quartz, K-feldspar, plagioclase, and biotite fragments in
311 a matrix of brown clay minerals. Cataclasite YDA-4 mainly consists of ≤ 0.2 -mm-diameter
312 quartz, K-feldspar, plagioclase, and biotite fragments in a clay mineral matrix. Conversely,
313 protolith sample YK-1 is mainly composed of quartz, plagioclase, K-feldspar, and biotite (≤ 5 -
314 mm-diameter crystals).

315

316 **3 Density, porosity, and effective atomic number**

317 **3.1 Measurement method**

318 Different methods were employed to obtain density measurements for the protolith and fault
319 rock samples since the fault rock samples generally contained many voids. The density analysis
320 for the protolith samples was performed according to the standard Japanese test method for
321 determining the bulk density of rocks (JGS2132-2009; The Japanese Geotechnical Society,
322 2017). The densities of the fault rock samples were determined via mercury intrusion
323 porosimetry (AutoPore IV 9500, Version 2.02; Micromeritics; Norcross, Georgia, USA) at the
324 Central Research Institute of Electric Power Industry (CRIEPI; Abiko-shi, Chiba, Japan); this
325 analysis also allowed an examination of the microcracks and pores within each sample.

326 The effective atomic number, Z_e , of a compound consisting of multiple types of atoms is defined

327 as:

$$328 \quad Z_e = (\sum f_i Z_i^{3.8})^{1/3.8}, \quad (1)$$

329 where f_i is the fraction of electrons on the i th atomic number species. For example, the effective

330 atomic number of a crystal composed of one silicon atom ($Z = 14$) and two oxygen atoms ($Z =$

331 8) is $(14/30 \times 14^{3.8} + 16/30 \times 8^{3.8})^{1/3.8} = 11.85$. Here we calculated the effective atomic number,

332 Z_{et} , of each sample based on the contents of the main components (SiO_2 , TiO_2 , Al_2O_3 , Fe_2O_3 ,

333 MnO , MgO , CaO , Na_2O , K_2O , and P_2O_5), which were measured via XRF analysis. Fused glass

334 bead samples underwent XRF analysis using a spectrometer at CRIEPI (XRF-1500, Rh X-ray

335 tube; Shimadzu Co., Ltd.; Nakagyo-ku, Kyoto, Japan) to obtain the Z_{et} values.

336

337 **3.2 Measurement results**

338 The density, ρ_t , porosity, ϕ , and Z_{et} measurement results are shown in Table 2 and Fig. 5, and

339 Table 3 contains the XRF analysis results, which were used to calculate Z_{et} .

340 There is a decrease in ρ_t as the youngest fault plane Y of every analyzed fault is approached

341 (Fig. 5a). There is an ~24% increase in ϕ as ρ_t decreases by 1 g/cm^3 , regardless of rock type

342 (fault rock or protolith; Fig. 5b). The mean ϕ values are 1.5% (standard deviation (SD) = 1.0%)

343 for the protolith, 12.6% (SD = 6.9%) for the cataclasite, 12.0% (SD = 4.8%) for the fault gouge

344 along the inactive faults, 17.4% (SD = 4.6%) for the fault gouge along the active faults, and
345 32.2% (no SD calculated since there were only two samples) for the fault breccia (Table 2).
346 However, every rock type yielded a positive correlation between ρ_t and Z_{et} (Fig. 5c), even
347 though the ρ_t and Z_{et} are expected to vary among different rock types. Fault breccia YDA-1 and
348 YDA-2 of the Yamada Fault both exhibit maximum ρ_t decreases of ~40%, whereas the Z_{et} values
349 are almost the same as that for protolith YK-1, which means that the relationship between ρ_t
350 and Z_{et} for the fault breccias is quite different from those of the other samples. This is because
351 YDA-1 and YDA-2 have been strongly affected by weathering, as evidenced by their dark-
352 brown color at outcrop and an Fe_2O_3 content of 4.28 wt%, which is much higher than those of
353 the fault gouge, cataclasite, and protolith samples (Table 3). Therefore, the fault breccia samples
354 were excluded from the subsequent study of the ρ_t – Z_{et} relationships among the collected rock
355 samples.

356 [<Table 2, Figure 5, Table 3](#)

357

358 **4 X-ray CT image analysis, and relationships among the CT** 359 **number, density, and effective atomic number**

360 We conducted X-ray CT image analysis on the fault rock and protolith samples to determine
361 how their CT values, which determine the degree of brightness of the CT image, may relate to

362 ρ_t and Z_{et} . We also attempted to quantitatively evaluate the characteristics of the fault rocks
363 using CT values. We analyzed 28 samples, excluding the fault breccia samples (YDA-1 and
364 YDA-2) because of their heterogeneity relative to the other samples.

365

366 **4.1 X-ray attenuation principle**

367 CT imaging captures the 3D X-ray attenuation distribution in a sample (e.g., Nakano et al.,
368 2000; Tsuchiyama et al., 2000; Ketchman and Carlson, 2001). The basic equation for the
369 attenuation of a monoenergetic beam through a homogeneous material is given by Beer's Law:

$$370 I = I_0 \exp(-\mu S),$$

371 (2)

372 where I_0 is the initial intensity of the incident X-ray beam, I is its emergent intensity, S is the
373 sample thickness, and μ is the linear X-ray attenuation coefficient (LAC) of the sample. The
374 LAC depends on both bulk density, ρ , and the atomic number, Z (Wellington and Vinegar,
375 1987):

$$376 \mu = \rho (a + bZ^{3.8}/E^{3.2}), \quad (3)$$

377 where E is the X-ray energy (keV), a is a nearly energy-independent coefficient this is termed
378 the Klein–Nishina coefficient, and b is a constant. Equation (3) is applicable for monochromatic
379 X-rays, such as those from a synchrotron radiation facility. However, this equation does not

380 hold for most commercial X-ray CT scanners, which use polychromatic X-ray beams, because
381 μ depends on the X-ray energy (e.g., Nakano et al., 2000; Tsuchiyama et al., 2000). The
382 photoelectric absorption of a compound consisting of multiple types of atoms is proportional to
383 the effective atomic number calculated via equation (1) (Wellington and Vinegar, 1987).

384 The CT number, N_{CT} , which determines the contrast of a CT image, is defined as:

$$385 \quad N_{CT} = 1000 \times (\mu - \mu_w) / \mu_w, \quad (4)$$

386 where μ_w is the X-ray attenuation coefficient of pure water. A polychromatic X-ray CT scanner
387 will allow μ to vary depending on the X-ray energy (effective energy), as described above. The
388 influence of the variations in μ with the energy differences in an X-ray energy distribution is
389 reduced by calculating N_{CT} , which is standardized using the μ ratio in equation (4). Substitution
390 of equation (3) into equation (4) therefore highlights the dependence of N_{CT} on ρ and Z_e when
391 the tube voltage and X-ray effective energy of a medical scanner are held constant.

392

393 **4.2 CT image analysis methods**

394 A CT image is essentially a bitmap of each pixel's CT number; however, it also contains various
395 artifacts due to the X-ray photography and image reconstruction. Therefore, the effects of these
396 artifacts, especially BH, must be eliminated or reduced to ensure the accuracy of the CT
397 numbers and therefore provide an accurate quantitative analysis.

398 BH artifacts cause the edges of a CT image to appear brighter than the center, such that the CT
399 numbers along the edges of a sample are greater than those in the center. This occurs because
400 the lower-energy X-rays are absorbed more readily than the higher-energy ones when
401 polychromatic X-rays pass through a sample near its center, where the transmission thickness
402 is large.

403 Geet et al. (2000) estimated the density, ρ , and effective atomic number, Z_e , via the dual-energy
404 method using a micro X-ray CT scanner. The μ_E coefficient, which is the effective LAC
405 corresponding to the effective energy of the X-rays, is derived from Eq. (3) as:

$$406 \quad \mu_E/\rho = A(E) + B(E)Z_e^{3.8}, \quad (5)$$

407 where A and B are constants depending E. The relationships among ρ , Z_e , and μ are expressed
408 as follows, using the A and B values calculated by approximating the relationship between μ_E/ρ
409 and $Z_e^{3.8}$ values at two different tube voltages:

$$410 \quad \rho = (B_h\mu_{E1} - B_l\mu_{Eh}) / (B_hA_l - B_lA_h) \quad (6)$$

411 and

$$412 \quad Z_e = [(A_l\mu_{Eh} - A_h\mu_{E1}) / (B_h\mu_{E1} - B_l\mu_{Eh})]^{(1/3.8)}, \quad (7)$$

413 where the h and l subscripts refer to the values derived from the high- and low-energy scans,
414 respectively.

415 Iwamori et al. (2020) used the dual-energy method (tube voltages: 140 and 100 kV) to analyze

416 the medical CT images of six different minerals with known densities and effective atomic
417 numbers (quartz, calcite, fluorite, rhodochrosite, cryptomelane, and hematite). They found that
418 the modal CT number, N_{CTM} , which is calculated from the two-dimensional (2D) CT image
419 whose peripheral CT values are excluded due to significant BH, could be used to estimate the
420 ρ and Z_e values of the mineral samples. Iwamori et al. (2020) also reported that the recorded
421 CT values for a single tube voltage (140 kV) can be used to estimate ρ and Z_e for the mineral
422 samples since these parameters possess a positive correlation.

423 We have already highlighted the positive correlation between ρ and Z_e for each analyzed fault
424 and rock type in this study (Fig. 5c). Therefore, we investigated the relationship among N_{CT} , ρ ,
425 and Z_e using the recorded CT images taken for a single tube voltage (140 kV).

426 We used a third-generation medical X-ray scanner (Aquilion Precision TSX-304A 160-row
427 multi-slice CT; Canon Medical Systems Co., Ltd.; Otawara, Tochigi, Japan) at CRIEPI. The
428 scanner has a 0.25-mm slice thickness and 0.098–0.313-mm pixel size. The X-ray tube has a W
429 target and a 0.4 mm \times 0.5 mm focal size. Three-dimensional CT images were acquired using a
430 single tube voltage (140 kV) and a 300-mAs tube current-time product. AIDR 3D (Canon
431 Medical Systems) was used for iterative approximation reconstruction (hybrid iterative
432 reconstruction method), with the FC30 reconstruction function employed. A CT image (1,024
433 \times 1,024 pixels) of an arbitrary 2D cross section near the center of the sample was extracted from

434 the 3D CT image. The effective energy of 140 kV was set to 64.1 keV based on Hubbell's
435 (1982) measurement results for fixed irradiation using an aluminum plate.

436

437 **4.3 Results**

438 Table 4 shows the X-ray CT image, density, and XRF analysis results. N_{CTM} was obtained from
439 the central part of each 2D CT image (within the white dotted perimeters in Fig. 6). The
440 periphery of each CT image, where BH is significant and determined relative to the median CT
441 value calculated for the entire arbitrary cross-sectional line (along the white dash-dotted line)
442 using the method outlined in Iwamori et al. (2020), was excluded.

443 <Table 4

444

445 **4.3.1 The MTL at the Hiji outcrop**

446 The CT images for sample HJ-8, which is from the fault fracture zone in the Sanbagawa Belt,
447 is dark at the fault gouge zones (HJ8-2, HJ8-3, and HJ8-4; Fig. 6a). The N_{CTM} values are in the
448 994–1109 range across the fault gouge, with the smallest value obtained within zone HJ8-3,
449 which is in contact with the main fault plane Y. The cataclasite zones (HJ8-1 and HJ8-5), which
450 are outside the fault gouge zones, appear brighter than the fault gouge, with N_{CTM} values in the
451 1281–1333 range.

452 The CT images for sample MZ-5, a pelitic schist protolith in the Sanbagawa Belt, exhibits a
453 striped pattern corresponding to planar schistosity (Fig. 6b) and possesses a N_{CTM} value of 2056.
454 A narrow band (≤ 1 mm wide) that is brighter than the rest of the image is inferred to be a
455 phengite vein, which has a greater effective atomic number than either quartz or albite.
456 Example histograms of the CT values in each of the sampled zones are shown in Fig. 6c–e.
457 Approximately 40,000–130,000 pixels are analyzed in each region, with the N_{CTM} values
458 generally following a normal distribution and possessing a standard deviation of 112–312
459 (Table 4). There may either be an increase in the frequency to values lower than N_{CTM} , or a
460 small side peak that is lower than N_{CTM} if the sample contains many cracks; however, N_{CTM}
461 corresponds to the CT value of the matrix, with the influence of cracks excluded.
462 Figure 6f and g show the CT value distributions along the white dash–dotted lines in the CT
463 image. We note that the $N_{CTM_{Median}}$ values (HJ-8: 991–1278, MZ-5: 2088) are almost consistent
464 with the N_{CTM} values that were calculated from the 2D CT images.
465 The $N_{CTM}-\rho_t$ relationship for Sanbagawa pelitic schist possesses a high positive correlation (ρ_t
466 $= 9.54 \times 10^{-4} N_{CTM} + 0.76$, $\gamma = 0.958$; Fig. 10a). The calculated density from this equation, ρ_c ,
467 is consistent with the real value, ρ_t , and possesses an error of $<9.5\%$ (Table 4).
468 The $N_{CTM}-Z_{et}$ relationship ($Z_{et} = 2.67 \times 10^{-4} N_{CTM} + 11.8$) can be derived from the
469 abovementioned $N_{CTM}-\rho_t$ relationship; the ρ_t-Z_{et} relationship is shown in Fig. 5c ($Z_{et} = 0.28\rho_t +$

470 11.6, $\gamma = 0.847$). The effective atomic number calculated from this equation, Z_{ec} , is consistent
471 with the real value, Z_{et} , and possesses an error of $<1.4\%$ (Table 4).

472 <Figure 6

473

474 **4.3.2 The MTL at the Awano–Tabiki outcrop**

475 The imaging results for samples AT, HA-1, and ATS-2 (Fig. 7a–c) are representative of the
476 seven samples (AT, ATR-2, ATR-3, ATR-4, ATS-1, ATS-2, and HA-1) collected from the
477 Awano–Tabiki outcrop.

478 The CT image for sample AT, which was taken from rocks in the fault fracture zone that formed
479 during the most recent fault activity, appears dark in the fault gouge (AT-2 and AT-3)
480 surrounding the main fault plane Y (Fig. 7a), with N_{CTM} values in the 1209–1665 range. The
481 smallest N_{CTM} value was observed in AT-2, which is in contact with the main fault plane Y. The
482 cataclasite samples (AT-1, AT-4, and AT-5), which are outside of the fault gouge zone, produce
483 brighter images than the fault gouge ones, with N_{CTM} values in the 1718–1864 range.

484 Sample HA-1, a Hatai tonalite protolith from the Ryoke Belt, possesses both dark-gray and
485 mottled white regions throughout the CT images (Fig. 7b), with a N_{CTM} value of 1908. A 1–2-
486 mm-thick band that appears brighter than the rest of the image is inferred to be hornblende and
487 chlorite, both of which have larger effective atomic numbers than quartz and plagioclase.

488 Sample ATS-2, a pelitic schist protolith from the Sanbagawa Belt, possesses striped patterns
489 corresponding to planar schistosity in the CT images (Fig. 7c), with a N_{CTM} value of 1961. A
490 narrow band (at most ~ 1 mm wide) that appears brighter than the rest of the image is inferred
491 to be a thin layer containing phengite and calcite, both of which have larger effective atomic
492 numbers than quartz.

493 Example CT value histograms for each zone are shown in Fig. 7d–h. Approximately 12,000–
494 200,000 pixels are analyzed in each zone, with the N_{CTM} values generally following a normal
495 distribution and possessing a standard deviation of 90–210 (Table 4). There may be a slight
496 increase in the frequency to values higher than N_{CTM} due to the influence of minerals with a
497 large effective atomic number in some instances; however, N_{CTM} corresponds to the CT value
498 of the matrix, with the influence of these minerals excluded.

499 Figure 7i–k shows the CT value distributions along the white dash–dotted line in the CT image.
500 We note that the $N_{CTM_{median}}$ values (AT: 1386–1801, HA-1: 1965, ATS-2: 1953) are almost
501 consistent with the N_{CTM} values calculated from the 2D CT images.

502 The $N_{CTM}-\rho_t$ relationships for the Sanbagawa pelitic schist and Ryoke tonalite possess high
503 positive correlations (pelitic schist: $\rho_t = 1.08 \times 10^{-3} N_{CTM} + 0.56$, $\gamma = 0.857$; tonalite: $\rho_t = 1.19$
504 $\times 10^{-3} N_{CTM} + 0.40$, $\gamma = 0.813$; Fig. 10b, c). The ρ_c values are consistent with the ρ_t values, and
505 possess errors of $<10.7\%$ (Table 4).

506 The N_{CTM} - Z_{et} relationships (pelitic schist: $Z_{et} = 1.57 \times 10^{-3} N_{CTM} + 9.47$; tonalite: $Z_{et} = 3.31 \times$
507 $10^{-3} N_{CTM} + 5.87$) can be derived from the abovementioned N_{CTM} - ρ_t relationships; the ρ_t - Z_{et}
508 relationships are shown in Fig. 5c (pelitic schist: $Z_{et} = 1.45\rho_t + 8.7$, $\gamma = 0.827$; tonalite: $Z_{et} =$
509 $2.78\rho_t + 4.76$, $\gamma = 0.802$). The Z_{ec} values are consistent with the Z_{et} values and possess errors of
510 $<7.9\%$ (Table 4).

511 <Figure 7

512

513 **4.3.3 The Tsuruga Fault at the Oritodani outcrop**

514 The CT results for samples T-3, K1, and T-5 (Fig. 8a–c) are representative of the five samples
515 (T-3, C-2, K-1, C-1, and T-5) collected from the Oritodani outcrop.

516 Sample T-3, which was taken from the rocks in the fault fracture zone that formed during the
517 most recent fault activity, appears dark in the fault gouge (T-3-1, T-3-2 and T-3-3) around the
518 main fault plane Y in the CT image (Fig. 8a), with N_{CTM} values in the 1185–1492 range. The
519 smallest N_{CTM} value is in T-3-3, which is in contact with the main fault plane Y. We consider T-
520 3-2 to be possibly affected by the most recent fault activity based on our abovementioned
521 analysis, but its N_{CTM} value is 1428, which is about the same as that in T-3-1 and exceeds that
522 in AT-2, a fault gouge along an inactive fault. Furthermore, the observed microstructures in T-
523 3 suggest that repetitive fault activity, which is indicative of an active fault, is limited to fault

524 gouge T-3-3. Therefore, we classify T-3-1 and T-3-2 as inactive fault gouge, and T-3-3 as active
525 fault gouge in this analysis. The cataclasite (T-3-4) outside of the fault gouge appears brighter
526 than the fault gouge, with a N_{CTM} value of 1622.

527 Sample K-1, a Koujaku granite protolith, possesses dark-gray and fine-grained white areas
528 throughout the CT images (Fig. 8b), with a N_{CTM} value of 1656. The small white areas (≤ 2 -mm
529 diameter) in the image are inferred to be biotite, which has a larger effective atomic number
530 than either quartz or plagioclase.

531 Sample T-5, which is a metabasalt protolith, is largely gray in the CT image, with the exception
532 of a white area at the upper right of the sample (Fig. 8c) and has a N_{CTM} value of 2590.

533 Example CT value histograms for each zone are shown in Fig. 8d–h. Approximately 20,000–
534 310,000 pixels are analyzed in each region, with the N_{CTM} values generally following a normal
535 distribution and possessing a standard deviation of 70–206 (Table 4). There may be a slight
536 increase in the frequency to values above N_{CTM} due to the influence of minerals with a large
537 effective atomic number in some instances, but N_{CTM} corresponds to the CT value of the matrix,
538 with the influence of these minerals excluded.

539 Figure 8i–k shows the CT value distributions along the white dash-dotted lines in the CT images
540 We note that the $N_{CTMedian}$ values (T-3: 1204–1553, K-1: 1706, ATS-2: 2612) are almost
541 consistent with the N_{CTM} values calculated from the 2D CT images.

542 The $N_{CTM}-\rho_t$ relationships for Koujaku granite and metabasalt have high positive correlations
543 (granite: $\rho_t = 1.23 \times 10^{-3} N_{CTM} + 0.45$, $\gamma = 0.872$; metabasalt: $\rho_t = 5.47 \times 10^{-4} N_{CTM} + 1.42$, $\gamma =$
544 0.967 ; Fig. 10d, e). The ρ_c values are the ρ_t values, and possess errors of $<3.7\%$ (Table 4).
545 The $N_{CTM}-Z_{et}$ relationships (granite: $Z_{et} = 2.83 \times 10^{-4} N_{CTM} + 11.6$; metabasalt: $Z_{et} = 7.66 \times 10^{-}$
546 $^4 N_{CTM} + 12.1$) can be derived from the abovementioned $N_{CTM}-\rho_t$ relationships; the ρ_t-Z_{et}
547 relationships are shown in Fig. 5c (granite: $Z_{et} = 0.23\rho_t + 11.5$, $\gamma = 0.528$; metabasalt: $Z_{et} =$
548 $1.40\rho_t + 10.1$, $\gamma = 0.669$). The Z_{ec} values are consistent with the Z_{et} values and possess errors of
549 $<3.7\%$ (Table 4).

550 <Figure 8

551

552 **4.3.4 The Yamada Fault at the Mushu outcrop**

553 Sample YDA, which is from the Miyazu granite in the fault fracture zone at the Mushu outcrop,
554 appears dark in the fault gouge of the CT image (YDA-3; Fig. 9a), with a N_{CTM} value of 1108.

555 The smallest N_{CTM} value is in YDA-3, which is adjacent to the main fault plane Y. The
556 cataclasite zone (YDA-4), which is outside of the fault gouge, is brighter than the fault gouge,
557 with a N_{CTM} value of 1333.

558 Sample YK-1, a Miyazu granite protolith, possesses dark-gray and fine-grained white areas
559 throughout the CT images (Fig. 9b), with a N_{CTM} value of 1730. The white area (≤ 2 -mm

560 diameter) in the image is inferred to be biotite, which has a larger effective atomic number than
561 both quartz and plagioclase.

562 Example CT value histograms for each zone are shown in Fig. 9c–e. Approximately 50,000–
563 330,000 pixels were analyzed in each region, with the N_{CTM} values generally following a normal
564 distribution and possessing a standard deviation of 119–224 (Table 4). There may be a slight
565 increase in the frequency to values above N_{CTM} due to the influence of minerals with a large
566 effective atomic number in some instances; however, N_{CTM} corresponds to the CT value of the
567 matrix, with the influence of these minerals excluded.

568 Fig. 9f and g show the CT value distributions along the white dash–dotted lines in the CT image.
569 We note that the $N_{CTMedian}$ values (YDA: 1105–1325, YK-1: 1782) are almost consistent with
570 the N_{CTM} values that were calculated from the 2D CT images.

571 The $N_{CTM}-\rho_t$ relationship for Miyazu Granite has a high positive correlation ($\rho_t = 9.79 \times 10^{-4}$
572 $N_{CTM} + 0.85$, $\gamma = 0.893$; Fig. 10f). The ρ_c value is consistent with ρ_t , and possesses an error
573 of <9.1% (Table 4).

574 The $N_{CTM}-Z_{et}$ relationship ($Z_{et} = 6.95 \times 10^{-4} N_{CTM} + 11.2$) can be derived from the
575 abovementioned $N_{CTM}-\rho_t$ relationship; the ρ_t-Z_{et} relationship is shown in Fig. 5c ($Z_{et} = 0.71\rho_t +$
576 10.6 , $\gamma = 0.975$). The Z_{ec} value is consistent with Z_{et} , and possesses an error of <0.7% (Table 4).

577 <Figure 9 <Figure 10

578

579 **5 Discussion**

580 We have concluded that N_{CTM} can be used to estimate ρ_t and Z_{et} for the protolith and fault rock
581 samples. Here we further investigate the ρ_t – ρ_c and Z_{et} – Z_{ec} relationships, in addition to the fault
582 rock characteristics based on the N_{CTM} –rock/protolith ratio (ρ_t and Z_{et}) relationship to validate
583 the feasibility of employing CT-based methods to characterize fault zones.

584

585 **5.1 ρ_t – ρ_c and Z_{et} – Z_{ec} relationships**

586 There is no significant difference in the ρ – ϕ relationship for various fault rock and protolith
587 types (Fig. 5b), whereas the trend of the ρ_t – Z_{et} relationship appears to be dependent on the
588 analyzed fault rock/protolith type (Fig. 5c). This indicates that N_{CTM} , which is a function of ρ
589 and Z_e , must be treated as an effective parameter for examining fault rock and protolith
590 characteristics by fault rock/protolith type. We observe strong correlations between ρ_c and ρ_t ,
591 and Z_{ec} and Z_{et} for each fault rock and protolith type, as shown in Fig. 11 (ρ : $\gamma = 0.944$, Z_e : $\gamma =$
592 0.895). Therefore, N_{CTM} , which is calculated by fault rock/protolith type, should be a reliable
593 parameter for calculating the ρ_t and Z_{et} values of a given rock sample and determining its fault
594 rock/protolith characteristics.

595

<Figure 11

596

597 **5.2 Fault rock characteristics based on the N_{CTM} –rock/protolith ratio (ρ_t and Z_{et})**

598 **relationship**

599 We have demonstrated that ρ_t , Z_{et} , and N_{CTM} all decrease as the main fault plane is approached

600 Furthermore, ρ_t is affected by Z_{et} , as shown in Fig. 5c, with a distinct ρ_t – Z_{et} relationship for each

601 fault and protolith type. Therefore, the effect of Z_{et} on ρ_t is suppressed by using the

602 rock/protolith density ratio of each fault and protolith type.

603 Table 5 shows the results of the analyzed fault rock characteristics based on the relationships

604 between N_{CTM} and the ρ_t and Z_{et} rock/protolith ratios. The statistics of the determined N_{CTM}

605 values and the ρ_t and Z_{et} rock/protolith ratios are provided in Table 6 and Fig. 12a–c.

606 [<Table 5](#) [<Table 6](#) [<Figure 12](#)

607 The N_{CTM} values (taken at 140 kV) were $\sim 1900 \pm 300$ for the protoliths, $\sim 1650 \pm 250$ for

608 cataclasite, $\sim 1450 \pm 200$ for the fault gouge along inactive faults, and $\sim 1100 \pm 100$ for the fault

609 gouge along active faults, as shown in Fig. 12a. Both the N_{CTM} values and N_{CTM} variations

610 decrease as the fault rock becomes more heavily deformed and the main fault plane is

611 approached.

612 The rock/protolith ρ_t ratio was $\sim 0.8 \pm 0.15$ for cataclasite and the fault gouge along inactive

613 faults, and $\sim 0.7 \pm 0.1$ for the fault gouge along active faults, as shown in Fig. 12b. The ρ_t ratio

614 decreases as the fault rock becomes more heavily deformed and the main fault plane is
615 approached, whereas the variation in the ρ_t ratio is approximately constant. Furthermore, the ρ_t
616 ratio differences among the different rock types are smaller than the N_{CTM} differences.

617 The rock/protolith Z_{et} ratio was ~ 0.85 , with no major difference between the analyzed fault rock
618 types, as shown in Fig. 12c. Therefore, Z_{et} is not closely related to the fault rock types, which
619 indicates that any distinct characteristics are dependent on differences in the protolith type (Fig.
620 5c).

621 This study demonstrates that analysis of the N_{CTM} values in CT images provides the best proxy
622 for detecting changes in fault rocks characteristics as the youngest active domain of a fault zone
623 is approached. Furthermore, the ρ_t ratio of the active fault is smaller than those of other fault
624 rocks, and the Z_{et} ratio decreases by $\sim 15\%$, regardless of the protolith type. This occurs because
625 N_{CTM} , which is a function of both ρ and Z_e , is affected by both the changes in ρ (dependent on
626 the fault rock type) and decreases in Z_e . This is also due to how N_{CTM} and the rock/protolith
627 ratios are calculated: N_{CTM} is calculated from more than 12,000 pixels of data by eliminating
628 the sample area due to the influence of cracks or minerals with a large effective atomic number,
629 with the rock/protolith ρ_t and Z_{et} ratios also calculated using only a portion of each sample area.

630 The N_{CTM} -rock/protolith ρ_t ratio relationship is shown in Fig. 12d. Both N_{CTM} and the
631 rock/protolith ρ_t ratio decrease as the main fault plane is approached and/or the degree of

632 fracturing increases. However, there is significant overlap between the $N_{CTM}-\rho_t$ ratio
633 distribution areas for the fault gouge along the inactive fault and cataclasite, making it difficult
634 to classify them using N_{CTM} and the ρ_t ratio. However, there is no overlap between the N_{CTM}
635 values for the fault gouges along active and inactive faults. Therefore, there is a possibility that
636 both fault rocks can be classified when $N_{CTM} \approx 1200$ is set as the boundary, which remains a
637 future task in its application to the classification of active faults and inactive faults.

638 The youngest active domain of a fault zone can be recognized as the area with the smallest
639 N_{CTM} and rock/protolith ρ_t ratio. It is expected that the accuracy of the ρ_t and Z_{et} values obtained
640 from the CT values in the fault fracture zone will be further enhanced as more studies conduct
641 CT analyses on both active and inactive faults, and a greater diversity of protoliths.

642

643 **6 Conclusions**

644 This study considered fault rock and protolith samples that were derived from pelitic schist,
645 tonalite, metabasalt, and granite along active faults (MTL, and Tsuruga and Yamada faults) and
646 an inactive fault (MTL). The density, porosity, and effective atomic number were determined
647 for the different fault and protolith types, and relationships among the CT value, density, and
648 effective atomic number were investigated. Our major findings and conclusions are as follows.

649 (1) The fault rock density, ρ_t , decreases as it approaches the youngest active fault plane, and the

650 porosity, ϕ , tends to increase by $\sim 24\%$ as ρ_t decreases by 1 g/cm^3 , regardless of the fault rock
651 or protolith type.

652 (2) The mean ϕ values are 1.5% (SD = 1.0%) for the protoliths, 12.6% (SD = 6.9%) for
653 cataclasite, 12.0% (SD = 4.8%) for the fault gouge along the inactive fault, 17.4% (SD = 4.6%)
654 for the fault gouge along the active faults, and 32.2% for the fault breccia.

655 (3) There is a positive correlation between ρ_t and the effective atomic number, Z_{et} , which is
656 unique to each fault and protolith type.

657 (4) The modal CT number, N_{CTM} , which is calculated from a 2D CT image (excluding the
658 periphery where BH is significant, and the influences of cracks and minerals with a large
659 effective atomic number) can be used to estimate the ρ_t and Z_{et} values of the protolith and fault
660 rock samples.

661 (5) The N_{CTM} values were $\sim 1900 \pm 300$ for the protolith, $\sim 1650 \pm 250$ for cataclasite, $\sim 1450 \pm$
662 200 for fault gouge in the inactive fault, and $\sim 1100 \pm 100$ for fault gouge in the active faults.

663 Both N_{CTM} and the variation in N_{CTM} decreased near the main fault plane. There is a possibility
664 that both fault rocks can be classified with $N_{CTM} \approx 1200$ as the boundary, which remains a future
665 task in its application to the classification for active and inactive faults.

666 (6) The rock/protolith density ratio was $\sim 0.8 \pm 0.15$ for cataclasite and fault gouge along the
667 inactive fault, and $\sim 0.7 \pm 0.1$ for fault gouge along the active faults.

668 (7) The change in fault rock characteristics due to the transition to the youngest active domain
669 of the fault zone is more distinct when analyzing N_{CTM} , which is a function of the ρ_t and Z_{et} ,
670 than the rock/protolith (ρ_t and Z_{et}) ratios.

671 (8) The youngest active domain of a fault zone can be recognized as the fault rock area with the
672 smallest N_{CTM} and rock/protolith ρ_t ratio.

673

674

675 **Declarations**

676 **Availability of data and material**

677 Data sharing not applicable to this article as no datasets were generated now. Please contact
678 author for data requests.

679

680 **Competing interests**

681 The authors of this article declare that they have no competing interest.

682

683 **Funding**

684 This work was funded by Kansai Electric Power Co. Inc..

685

686 **Authors' contributions**

687 AI proposed this study and performed compilation and interpretation on all analysis results. HT
688 provided support and guidance for all analyzes and interpretation of analysis results. NA
689 captured CT images and performed XRF analysis. TS took the lead in sampling of fault rocks.
690 EN, SN and KU collaborated with the corresponding author to interpret analysis results. All
691 authors read and approved the final manuscript.

692

693 **Acknowledgements**

694 We thank Seiji Matayoshi and Yasuhiro Yamada for their assistance with the analyses at CRIEPI.
695 We are grateful to Tadahiro Nishizaki for his assistance during the sample collection in the field.
696 Kana Tanabe, Shotaro Yamamoto, Kozo Kiyose, Koichi Hojo, and Koudai Kuramoto provided
697 careful guidance during the X-ray effective energy measurements and CT imaging.

698

699 **References**

700 Aiyama K, Tanaka S, Sasaki T (2017) Consideration of the Activity of a Fault Based on Detailed
701 Structural Analysis of a Fault Fracture Zone: Case Study of the Yamada Fault, Western Japan.
702 J. Japan Soc. Eng. Geol., 58. 1, 2–18.*
703 Boespflug X, Long BFN, Occhietti S (1995) CAT-scan in marine stratigraphy: a quantitative

704 approach. *Marine Geol.* 122, 281-301.

705 Earthquake Research Committee (2004) Long-term evaluation of the Yamada Fault Zone. The
706 Headquarters for Earthquake Research Promotion.
707 https://www.jishin.go.jp/main/chousa/katsudansou_pdf/74_yamada.pdf/*

708 Geet MV, Swennen R, Wevers M (2000) Quantitative analysis of reservoir rocks by microfocus
709 X-ray computerized tomography. *Sedimentary Geol.*, 132, 25-36

710 Hirono T, Sakaguchi M, Otsuki K, Sone H, Fujimoto K, Mishima T, Lin W, Tanikawa W,
711 Tanimizu M, Soh W, Yeh E, Song S (2008) Characterization of slip zone with the 1999 Taiwan
712 Chi-Chi earthquake: X-ray CT image analyses and microstructural observation of the Taiwan
713 Chelungpu fault. *Tectonophysics.* 449, 63–84.*

714 Hounsfield GN (1973) Computerized transverse axial scanning (tomography): Part I .
715 Description of system. *British J. Radiology*, 46, 1016–1022.

716 Hubbell JH (1982) Photon mass attenuation and energy-absorption coefficients from 1 keV to
717 20 MeV. *Int. J. Appl. Radiat. Isot.* 33, 1269-1290.

718 Ikeda R, Omura K, Iio Y, Arai T, Kobayashi K, Matsuda T, Shimada K, Tanaka H, Tomita T,
719 Hirano S (2001) Drilling investigation through the Nojima Fault of the 1995 Hyogo-ken Nanbu
720 Earthquake, Japan. National Research Institute for Earth Science and Disaster Prevention
721 Research Report, 61, 141-153.*

722 Iwamori A, Sasaki T, Sugimori T, Aiyama K, Goto N, Yanagida M, Shigemitsu Y, Tanaka Y
723 (2015) Activity history of the Yamada fault in the late Quaternary -Outcrop survey at Mushu,
724 Tanto-cho. Proceedings of the 2015 Autumn Meeting of the Active Fault Society of Japan, 62-
725 63.*

726 Iwamori A, Takagi H, Asahi N, Sugimori T, Nakata E, Nohara S, Ueta K (2020) Development
727 of a method for presuming the density and effective atomic number of mineral samples by
728 utilizing medical X-ray CT scanning. Jap. Mag. Mineral. Petrol. Sci., 49, 101-117. *

729 Ketchman RA, Carlson WD (2001) Acquisition, optimization and interpretation of X-ray
730 computed tomographic imagery: applications to the geosciences. Comp. Geosci. 27, 381–400.

731 Ketchman RA, Hanna RD (2014) Beam hardening correction for X-ray computed tomography
732 of heterogeneous natural materials. Comp. Geosci. 67, 49-61.

733 Kurimoto C, Naito K, Sugiyama Y, Nakae S (1999) Geological map of Japan 1:50,000, Tsuruga,
734 National Institute of Advanced Industrial Science and Technology.*

735 Mizoguchi K, Ueta K (2012) Evaluation of fault activity based on fault-zone properties –
736 Microfracture analysis of damage zone along an active fault located east of epicentral area of
737 the 1943 Tottori Earthquake, Japan -. Civil Engin. Res. Lab. Rep. No. N11041, 17 pp.*

738 Morrow CA, Lockner DA (2001) Hayward fault rocks: Porosity, density and strength
739 measurements. U.S. Department of the Interior, USGS Open-File Report 2001-421

740 Nakano T, Nakashima Y, Nakamura K, Ikeda S (2000) Observation and analysis of internal
741 structure of rock using X-ray CT. *J. Geol. Soc. Japan* 106, 363–378.*

742 National Institute of Advanced Industrial Science and Technology (2016) 151 Tsuruga
743 earthquake fault. Active fault database of Japan. <https://gbank.gsj.jp/activefault/>*

744 Nishioka Y, Nakae S, Takeuchi K, Banno Y, Mizuno K, Ozaki M, Nakashima R, Sanematsu K,
745 Nawa K, Komazawa M (2010) Geological map of Japan 1:200,000, Ise, National Institute of
746 Advanced Industrial Science and Technology.*

747 Nishizawa O, Nakano T, Noro H, Inazaki T (1995) Recent advances of X-ray CT technology
748 for analyzing geologic materials. *Bull. Geol. Surv. Japan* 46, 565–571.*

749 Okada A (1992) Proposal of the segmentation on the Median Tectonic Line active fault system.
750 *Mem. Geol. Soc. Japan.* 40, 15-30.*

751 Orsi TH, Edwards CM, Anderson AL (1994) X-ray computed tomography: A nondestructive
752 method for quantitative analysis of sediment cores. *J. Sed. Res.* A64, 690-693.

753 Raynaud S, Fabre D, Mezerolle F, Geraud Y, Latiere HJ (1989) Analysis of the internal structure
754 of rocks and characterization of mechanical deformation by a non-destructive method: X-ray
755 tomodensitometry. *Tectonophysics.* 159, 149-159

756 Shigematsu N, Kametaka M, Inada N, Miyawaki M, Miyakawa A, Kameda J, Togo T, Fujimoto
757 K (2017) Evolution of the Median Tectonic Line fault zone, SW Japan, during exhumation.

- 758 Tectonophysics. 696–697, 52–69.
- 759 Takagi H (1984) Mylonitic rocks along the Median Tectonic Line in Takato–Ichinose area,
760 Nagano Prefecture. *J. Geol. Soc. Japan.* 90, 81–100.*
- 761 Takagi H (1985) Mylonitic rocks of the Ryoike belt in the Kayumi area, eastern part of the Kii
762 Peninsula. *J. Geol. Soc. Japan.* 91, 637–651.*
- 763 Takagi H, Kobayashi K (1996) Composite planar fabrics of fault gouges and mylonites—
764 comparative petrofabrics. *J. Geol. Soc. Japan* 102, 170–179.*
- 765 Takagi H, Sugiyama K, Tamura I, Mizuno K, Kitazawa N, Kawamoto K (2019) Identification
766 of the youngest activity of the Median Tectonic Line at Hiji outcrop, Ina City, Nagano
767 Prefecture. *Active Fault Res.* 50, 1–12.*
- 768 Takeuchi F, Nakamura K, Matsumura K, Watanabe K (2005) Density of stones observed near
769 and around the Yamazaki Fault System. *Annals of Disas. Prev. Res. Inst., Kyoto Univ.*, 48B.*
- 770 Tanaka Y, Kametaka M, Okazaki K, Suzuki K, Seshimo K, Aoki K, Shimada K, Watanabe T,
771 Nakayama K (2018) Examination of Evaluation Method for Fault Activity Based on
772 Morphological Observation of Fault Planes. *J. Japan Soc. Eng. Geol.*, 59. 1, 13–27.*
- 773 The Japanese Geotechnical Society (2017) Japanese Geotechnical Society Standards Vol. 2–
774 Laboratory Testing Standards of Geomaterials, 300p.*
- 775 Tsuchiyama A, Uesugi K, Nakano T (2000) A Study of three-dimensional structures of rocks

776 and minerals using a high-resolution X-ray CT method—primitive materials in the solar system
777 and chondrules. *J. Geogr. (Chigaku Zasshi)* 109, 845–858.*
778 Ueta K, Tani K, Kato T (2000) Computerized X-ray tomography analysis of three-dimensional
779 fault geometries in basement-induced wrench faulting. *J. Eng. Geol.* 56, 197-210.
780 Verhelst F, David P, Fermont W, Jegers L, Vervoort A (1996) Correlation of 3D-computerized
781 tomographic scans and 2D-colour image analysis of Westphalian coal by means of multivariate
782 statistics. *Int. J. Coal Geol.* 29, 1–21.
783 Wellington SL, Vinegar HJ (1987) X-ray computerized tomography. *J. Petrol. Tech.* 39, 885–
784 898.

785

786 * in Japanese with English abstract.

787

788

789 **Figure legends**

790 Figure 1. Simplified geotectonic map showing the location of the study area around the MTL
791 and the Tsuruga and Yamada faults. The stars denote the approximate locations where the
792 samples were collected; see Fig. 2 for further details on each sample site.

793

794 Figure 2. Geological maps of the area around (a) the MTL in the Ina area, (b) the MTL in the
795 Matsusaka area, (c) the Tsuruga Fault, and (d) the Yamada Fault. These maps have been
796 simplified and partly modified after the 1/200,000 geological maps from the National Institute
797 of Advanced Industrial Science and Technology (AIST): (a) Kofu (2002), (b) Ise (2010), (c)
798 Gihu (1992), and (d) Miyazu (1968). The stars denote the approximate locations of fault
799 outcrops and where the samples were collected.

800

801 Figure 3. Photographs of the outcrop (a, e), and polished slab (b, f) of the observed brittle fault
802 rocks taken perpendicular to the fault plane and parallel to the lineations, and photomicrographs
803 (c, d, g, h; cross-polarized light) of the fault rock samples. (a) The Hiji outcrop of the MTL. (b)
804 HJ8. (c) HJ8-1. (d) HJ8-3. (e) The Awano–Tabiki outcrop of the MTL. (f) AT. (g) AT-1–AT-2–
805 AT-4. (h) AT-2–AT-4. The stereoplots show the orientation of fault plane γ and the direction of
806 slip in the zone formed during the most recent fault movements (a, e). Abbreviations in (g) and
807 (h): P: P-foliation; R_1 : Riedel shear; P_n , P_r : P foliations showing normal and reverse senses of
808 shear, respectively; R_{1n} , R_{1r} : Riedel shear showing normal and reverse senses of shear,
809 respectively.

810

811 Figure 4. Outcrop photographs (a, f), observed brittle fault rocks in the outcrops, photographs

812 taken perpendicular to the fault plane and parallel to the lineations (b, g), and photomicrographs
813 of the fault rock and protolith samples (c, d, e, h, i: cross-polarized light). (a) The Oritodani
814 outcrop of the Tsuruga Fault. (b) T-3. (c) T-3-2–T-3-3. (d) T-3-2. (e) T-3-3. (f) The Mushu
815 outcrop of the Yamada Fault. (g) YDA. (h) YDA-4. (i) YDA-2–YDA-3. Stereoplots show the
816 orientation of fault plane Y and slip direction in the zone formed during the most recent fault
817 movements (a, f). Abbreviations: P: P-foliation; R₁: Riedel shear.

818

819 Figure 5. Density, porosity, and effective atomic number measurement results. (a) Relationship
820 between fault rock type and real density, ρ_t . (b) Crossplot of porosity, ϕ , versus ρ_t . (c) Crossplot
821 of effect atomic number, Z_{et} , versus ρ_t .

822

823 Figure 6. X-ray CT image analysis results for the Hiji outcrop samples. CT images of samples
824 (a) HJ-8 and (b) MZ-5. CT number histograms for (c) HJ8-1, (d) HJ8-3, and (e) MZ-5. The
825 modal CT number, N_{CTM} , for each zone was calculated near the center (within the white dotted
826 line), with the peripheral CT numbers excluded. CT number profiles for (f) HJ-8 and (g) MZ-
827 5, with the values calculated along the dash–dotted lines in (a) and (b), respectively.

828

829 Figure 7. X-ray CT image analysis results for the Awano–Tabiki outcrop samples. CT images

830 of the (a) AT, (b) HA-1, and (c) ATS-2 samples. CT number histograms for the (d) AT-1, (e) AT-
831 2, (f) AT-4, (g) HA-1, and (h) ATS-2 samples. The N_{CTM} value for each zone was calculated
832 near the center (within the white dotted lines in (a)–(c)), with the peripheral areas excluded. CT
833 number profiles for (i) AT, (j) HA-1, and (k) ATS-2, with the values calculated along the dash-
834 dotted lines in (a)–(c), respectively.

835

836 Figure 8. X-ray CT image analysis results for the Oritodani outcrop samples. CT images of
837 samples (a) T-3, (b) K-1, and (c) T-5. CT number histograms for (d) T-3-1, (e) T-3-3, (f) T-3-4,
838 (g) K-1, and (h) T-5. The N_{CTM} value in each zone was calculated near the center (within the
839 white dotted lines in (a)–(c)), with the peripheral values excluded. CT number profiles for (i)
840 T-3, (j) K-1, and (k) T-5, with the values calculated along the dash-dotted lines in (a)–(c),
841 respectively.

842

843 Figure 9. X-ray CT image analysis results for the Mushu outcrop samples. CT images of the (a)
844 YDA and (b) YK-1 samples. CT number histograms for (c) YDA-3, (d) YDA-4, and (e) YK-1.
845 The N_{CTM} values were calculated near the center (within the white dotted lines in (a) and (b))
846 of each zone, with the peripheral areas excluded. CT number profiles for (f) YDA and (g) YK-
847 1, with the values calculated along the dash-dotted lines in (a) and (b), respectively.

848

849 Figure 10. ρ_t - N_{CTM} crossplots for the sampled fault rocks and protoliths. (a) Schist (Hiji
850 outcrop). (b) Schist (Awano–Tabiki outcrop). (c) Tonalite (Awano–Tabiki outcrop). (d) Granite
851 (Oritodani outcrop). (e) Metabasalt (Oritodani outcrop). (f) Granite (Mushu outcrop).

852

853 Figure 11. Crossplots of (a) the real density, ρ_t , versus the measured density, ρ_c , which is
854 calculated from N_{CTM} , and (b) the real effective atomic number, Z_{et} , versus the measured
855 effective atomic number, Z_{ec} , which is calculated from N_{CTM} . Regression lines were determined
856 via least-squares analysis.

857

858 Figure 12. Box plots of (a) N_{CTM} , (b) rock/protolith ρ_t ratio, (c) and rock/protolith $Z_{et}^{3.8}$ ratio,
859 and (d) crossplot of N_{CTM} versus rock/protolith ρ_t ratio.

860

861 **Tables**

862 Table 1. Locations and fault/protolith details of the analyzed samples. See Figs 1 and 2 for
863 sample locations.

864

865 Table 2. Density, porosity, and XRF analysis results.

866

867 Table 3. XRF analysis and effective atomic number (Z_{et}) results for the rock samples.

868

869 Table 4. Relationship among N_{CTM} (calculated from the CT images at 140kV), ρ_t , and Z_{et} for
870 each of the samples.

871

872 Table 5. Comparison of ρ_t , Z_{et} , N_{CTM} , and the rock/protolith ratios (ρ_t and $Z_{et}^{3.8}$) for each of the
873 analyzed samples.

874

875 Table 6. Statistics of the determined N_{CTM} values and rock/protolith ratios (ρ_t and $Z_{et}^{3.8}$).

876

Figures

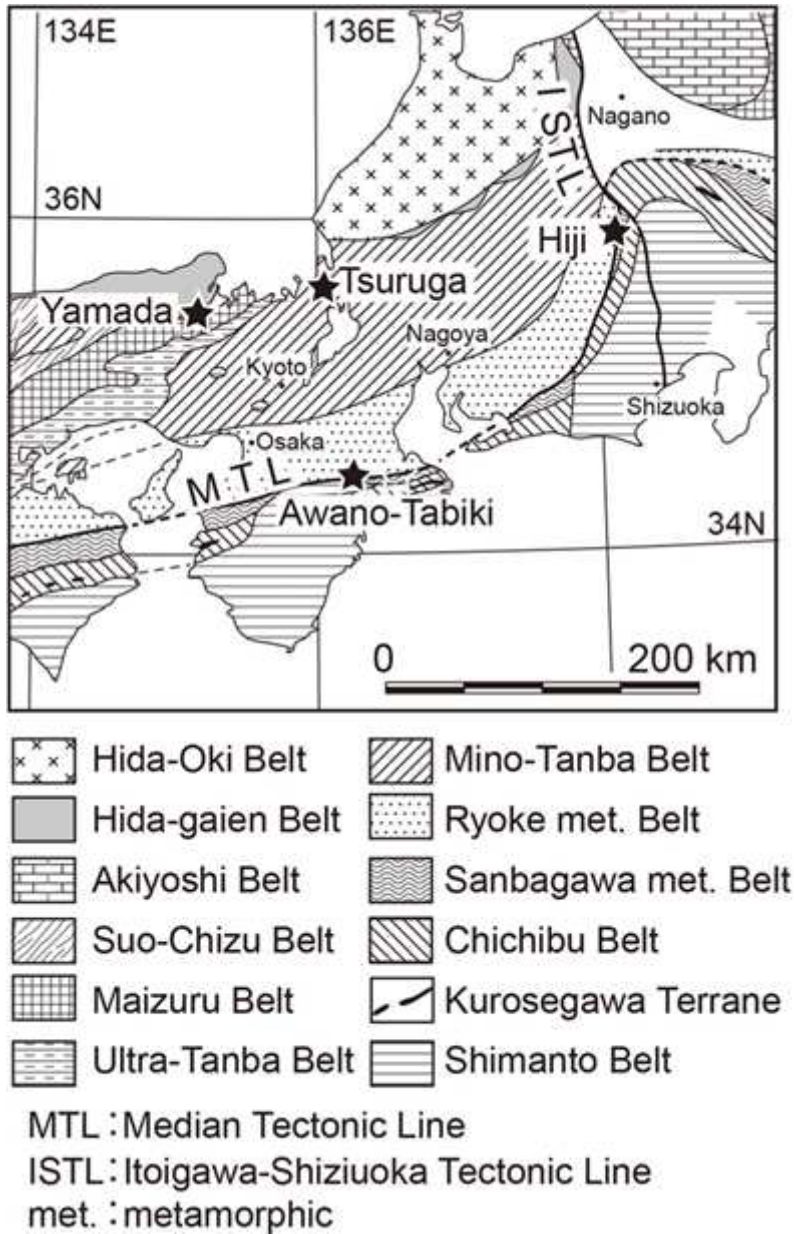


Figure 1

Simplified geotectonic map showing the location of the study area around the MTL and the Tsuruga and Yamada faults. The stars denote the approximate locations where the samples were collected; see Fig. 2 for further details on each sample site. Note: The designations employed and the presentation of the material on this map do not imply the expression of any opinion whatsoever on the part of Research Square concerning the legal status of any country, territory, city or area or of its authorities, or concerning the delimitation of its frontiers or boundaries. This map has been provided by the authors.

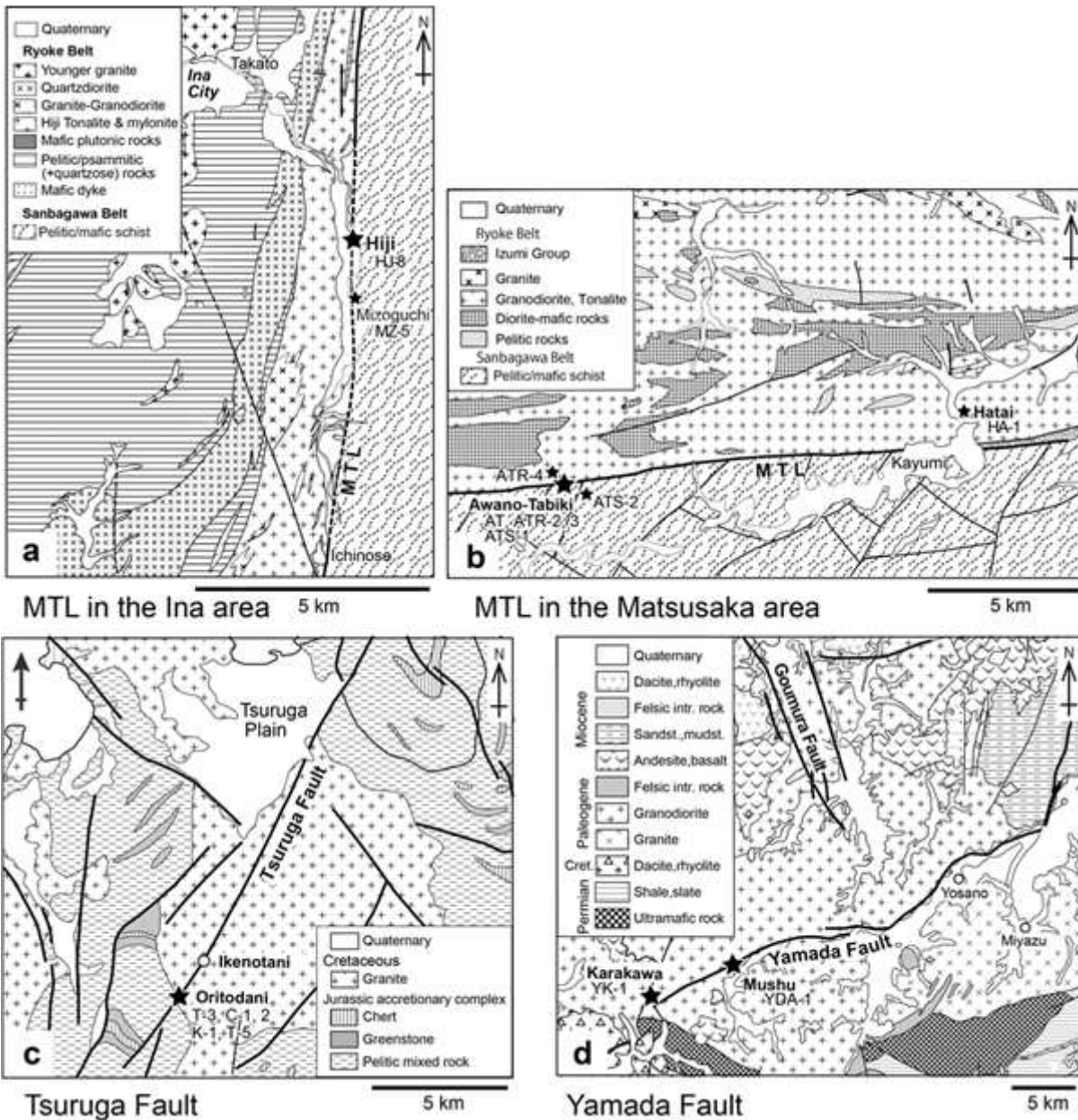


Figure 2

Geological maps of the area around (a) the MTL in the Ina area, (b) the MTL in the Matsusaka area, (c) the Tsuruga Fault, and (d) the Yamada Fault. These maps have been simplified and partly modified after the 1/200,000 geological maps from the National Institute of Advanced Industrial Science and Technology (AIST): (a) Kofu (2002), (b) Ise (2010), (c) Gihu (1992), and (d) Miyazu (1968). The stars denote the approximate locations of fault outcrops and where the samples were collected. Note: The designations employed and the presentation of the material on this map do not imply the expression of any opinion whatsoever on the part of Research Square concerning the legal status of any country, territory, city or area or of its authorities, or concerning the delimitation of its frontiers or boundaries. This map has been provided by the authors.

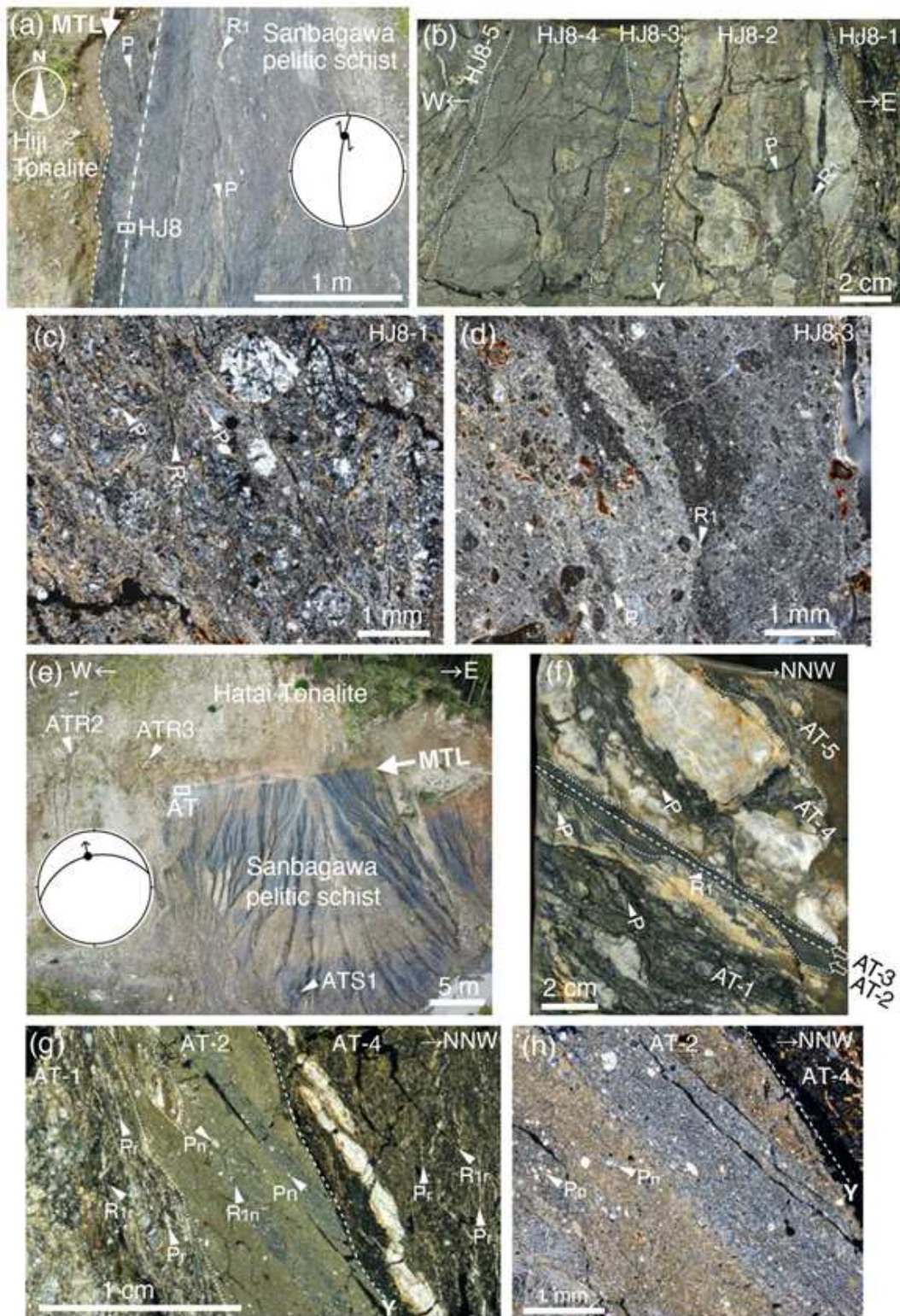


Figure 3

Photographs of the outcrop (a, e), and polished slab (b, f) of the observed brittle fault rocks taken perpendicular to the fault plane and parallel to the lineations, and photomicrographs (c, d, g, h; cross-polarized light) of the fault rock samples. (a) The Hiji outcrop of the MTL. (b) HJ8. (c) HJ8-1. (d) HJ8-3. (e) The Awano-Tabiki outcrop of the MTL. (f) AT. (g) AT-1-AT-2-AT-4. (h) AT-2-AT-4. The stereoplots show the orientation of fault plane Y and the direction of slip in the zone formed during the most recent

Outcrop photographs (a, f), observed brittle fault rocks in the outcrops, photographs taken perpendicular to the fault plane and parallel to the lineations (b, g), and photomicrographs of the fault rock and protolith samples (c, d, e, h, i: cross-polarized light). (a) The Oritodani outcrop of the Tsuruga Fault. (b) T-3. (c) T-3-2–T-3-3. (d) T-3-2. (e) T-3-3. (f) The Mushu outcrop of the Yamada Fault. (g) YDA. (h) YDA-4. (i) YDA-2–YDA-3. Stereoplots show the orientation of fault plane Y and slip direction in the zone formed during the most recent fault movements (a, f). Abbreviations: P: P-foliation; R1: Riedel shear. Note: The designations employed and the presentation of the material on this map do not imply the expression of any opinion whatsoever on the part of Research Square concerning the legal status of any country, territory, city or area or of its authorities, or concerning the delimitation of its frontiers or boundaries. This map has been provided by the authors.

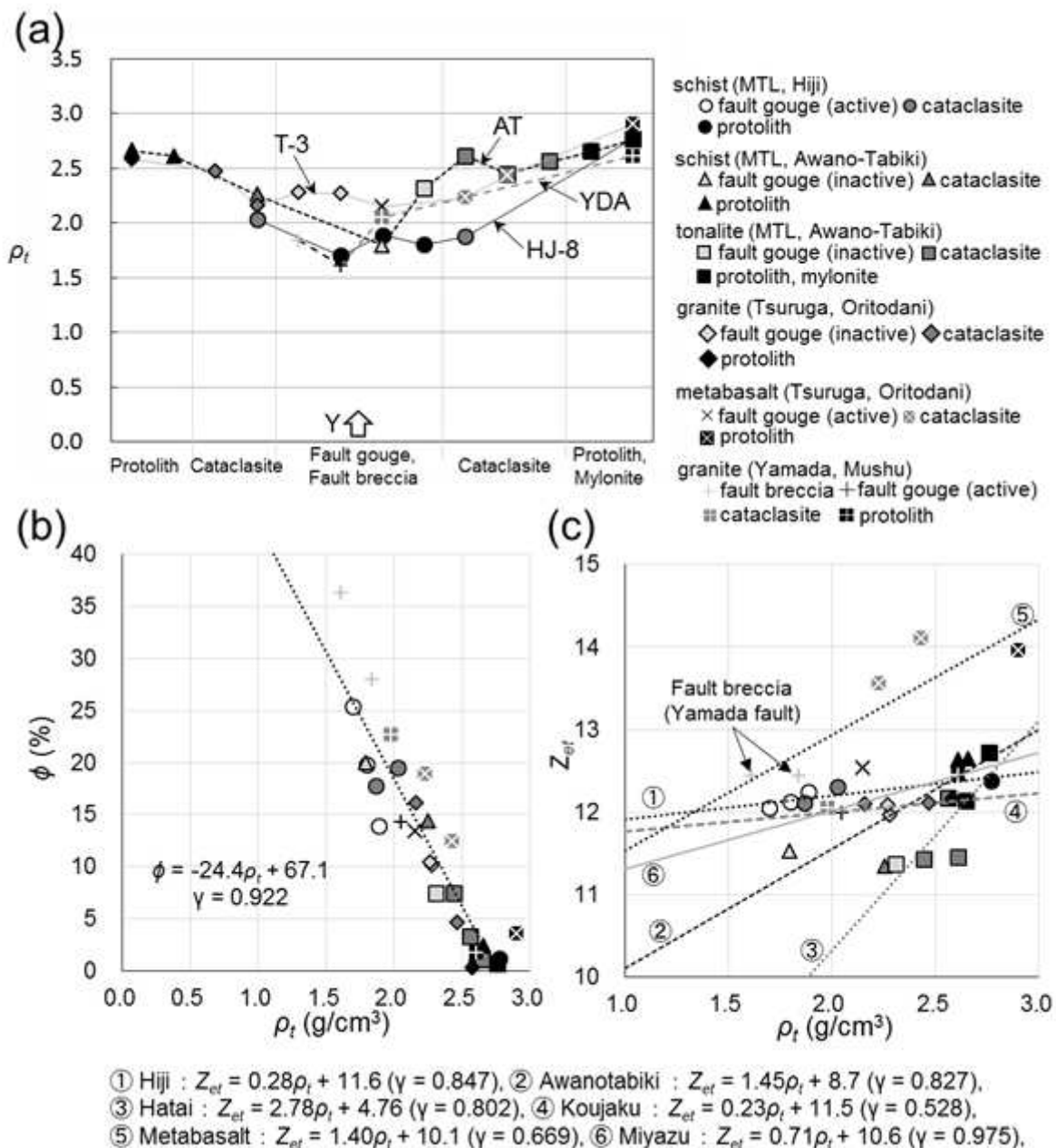


Figure 5

Density, porosity, and effective atomic number measurement results. (a) Relationship between fault rock type and real density, ρ_t . (b) Crossplot of porosity, ϕ , versus ρ_t . (c) Crossplot of effect atomic number, Z_{eff} , versus ρ_t .

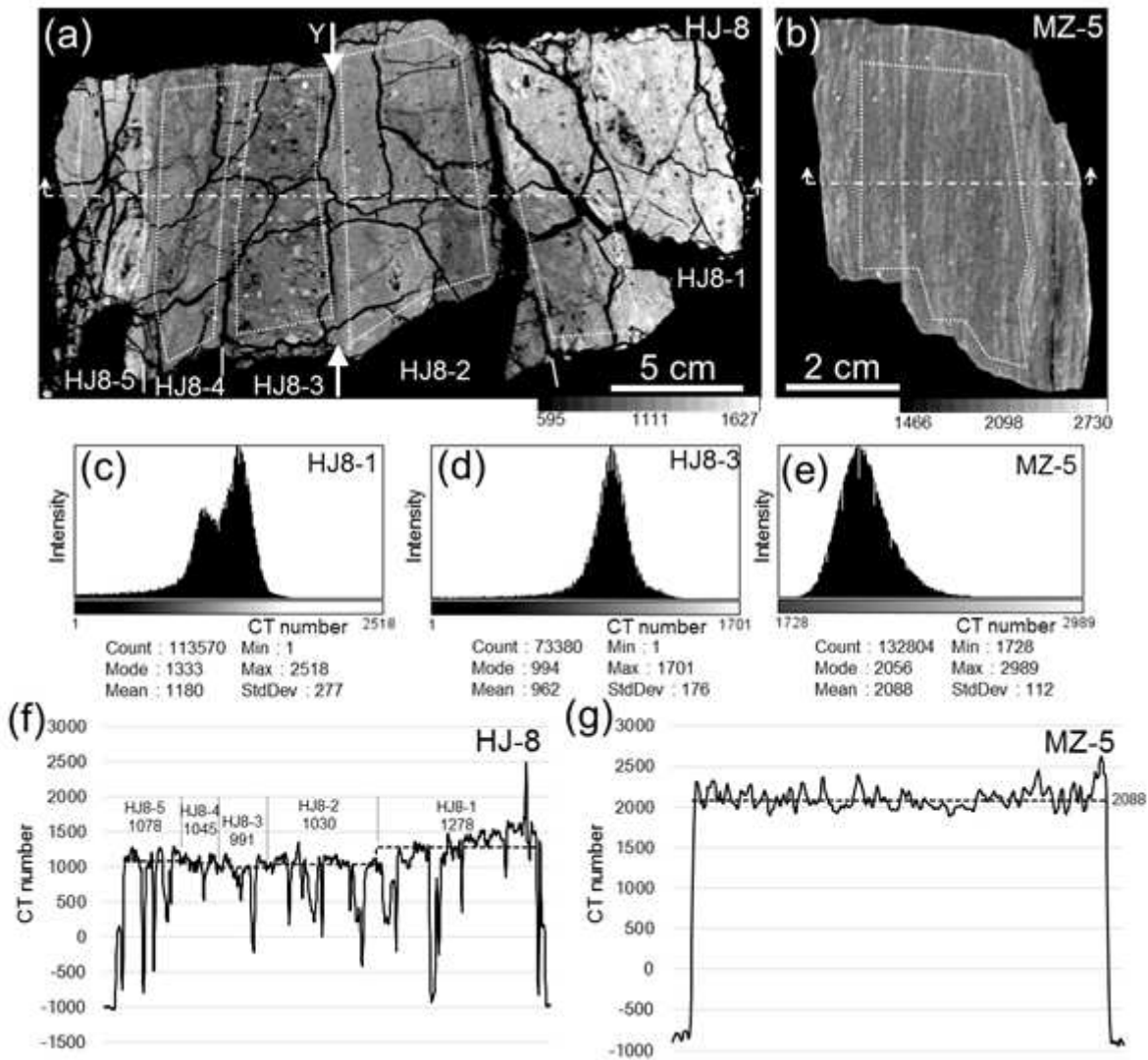


Figure 6

X-ray CT image analysis results for the Hiji outcrop samples. CT images of samples (a) HJ-8 and (b) MZ-5. CT number histograms for (c) HJ8-1, (d) HJ8-3, and (e) MZ-5. The modal CT number, NCTM, for each zone was calculated near the center (within the white dotted line), with the peripheral CT numbers excluded. CT number profiles for (f) HJ-8 and (g) MZ-5, with the values calculated along the dash-dotted lines in (a) and (b), respectively.

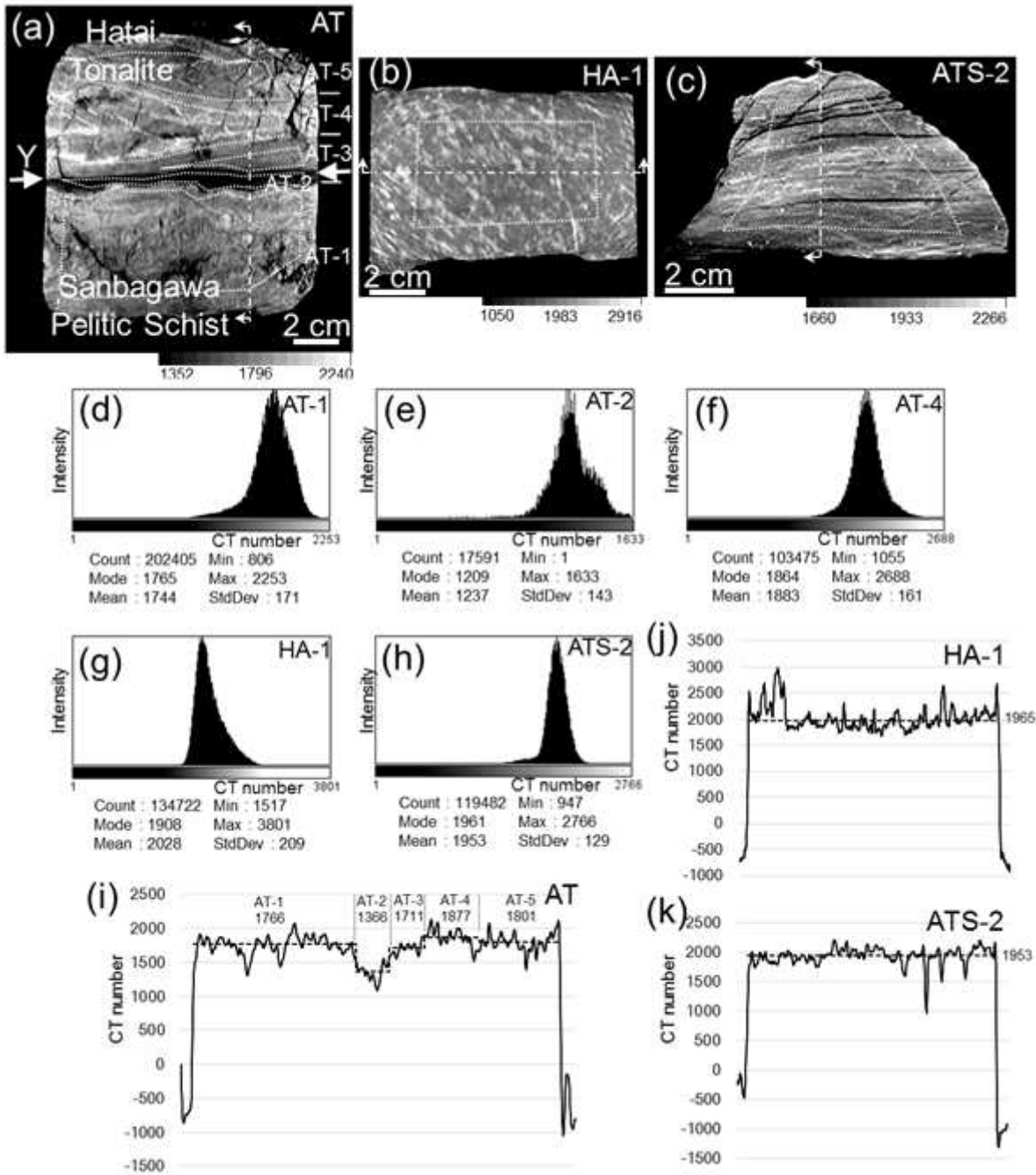


Figure 7

X-ray CT image analysis results for the Awano-Tabiki outcrop samples. CT images of the (a) AT, (b) HA-1, and (c) ATS-2 samples. CT number histograms for the (d) AT-1, (e) AT-2, (f) AT-4, (g) HA-1, and (h) ATS-2 samples. The NCTM value for each zone was calculated near the center (within the white dotted lines in (a)–(c)), with the peripheral areas excluded. CT number profiles for (i) AT, (j) HA-1, and (k) ATS-2, with the values calculated along the dash-dotted lines in (a)–(c), respectively.

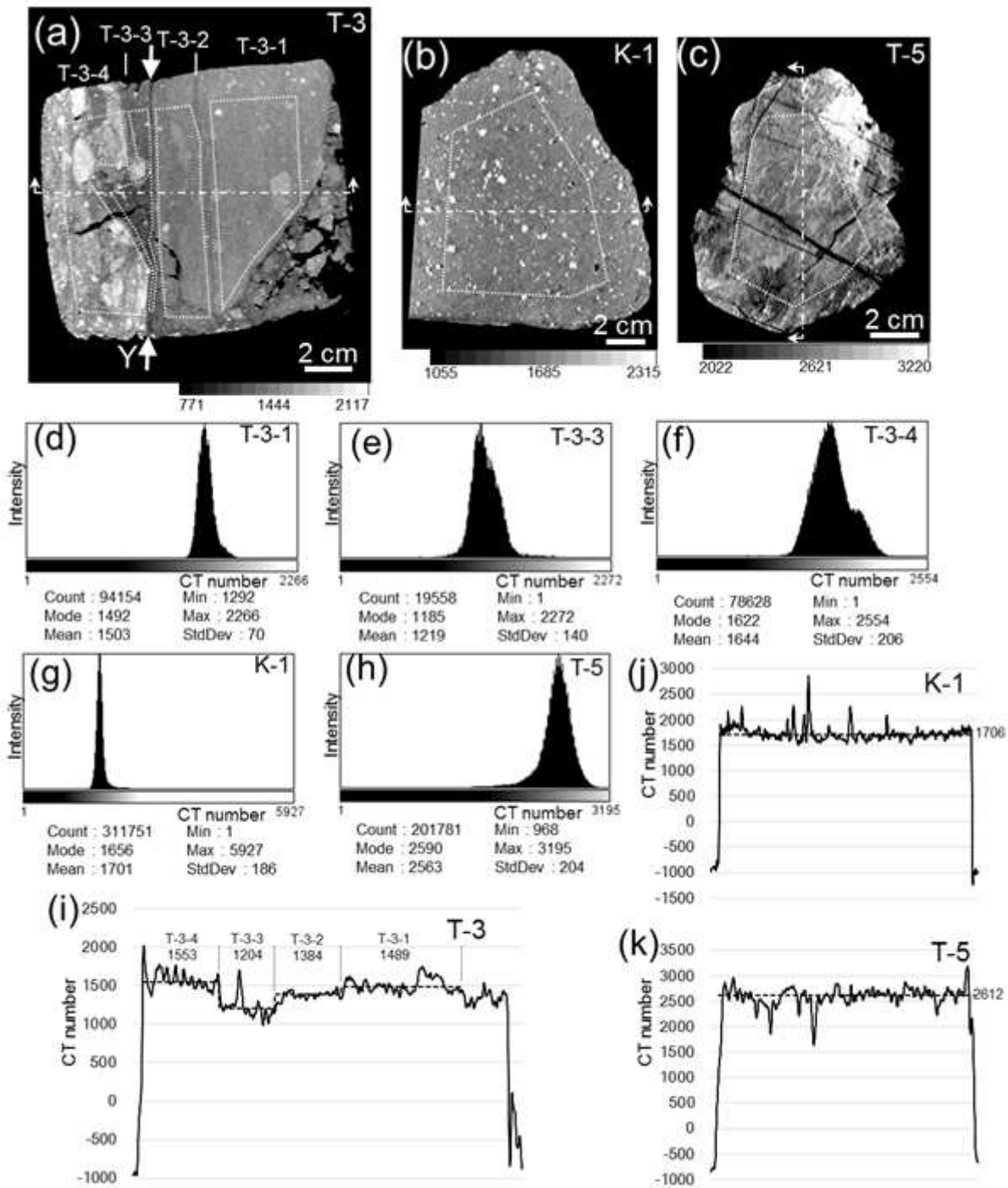


Figure 8

X-ray CT image analysis results for the Oritodani outcrop samples. CT images of samples (a) T-3, (b) K-1, and (c) T-5. CT number histograms for (d) T-3-1, (e) T-3-3, (f) T-3-4, (g) K-1, and (h) T-5. The NCTM value in each zone was calculated near the center (within the white dotted lines in (a)–(c)), with the peripheral values excluded. CT number profiles for (i) T-3, (j) K-1, and (k) T-5, with the values calculated along the dash-dotted lines in (a)–(c), respectively.

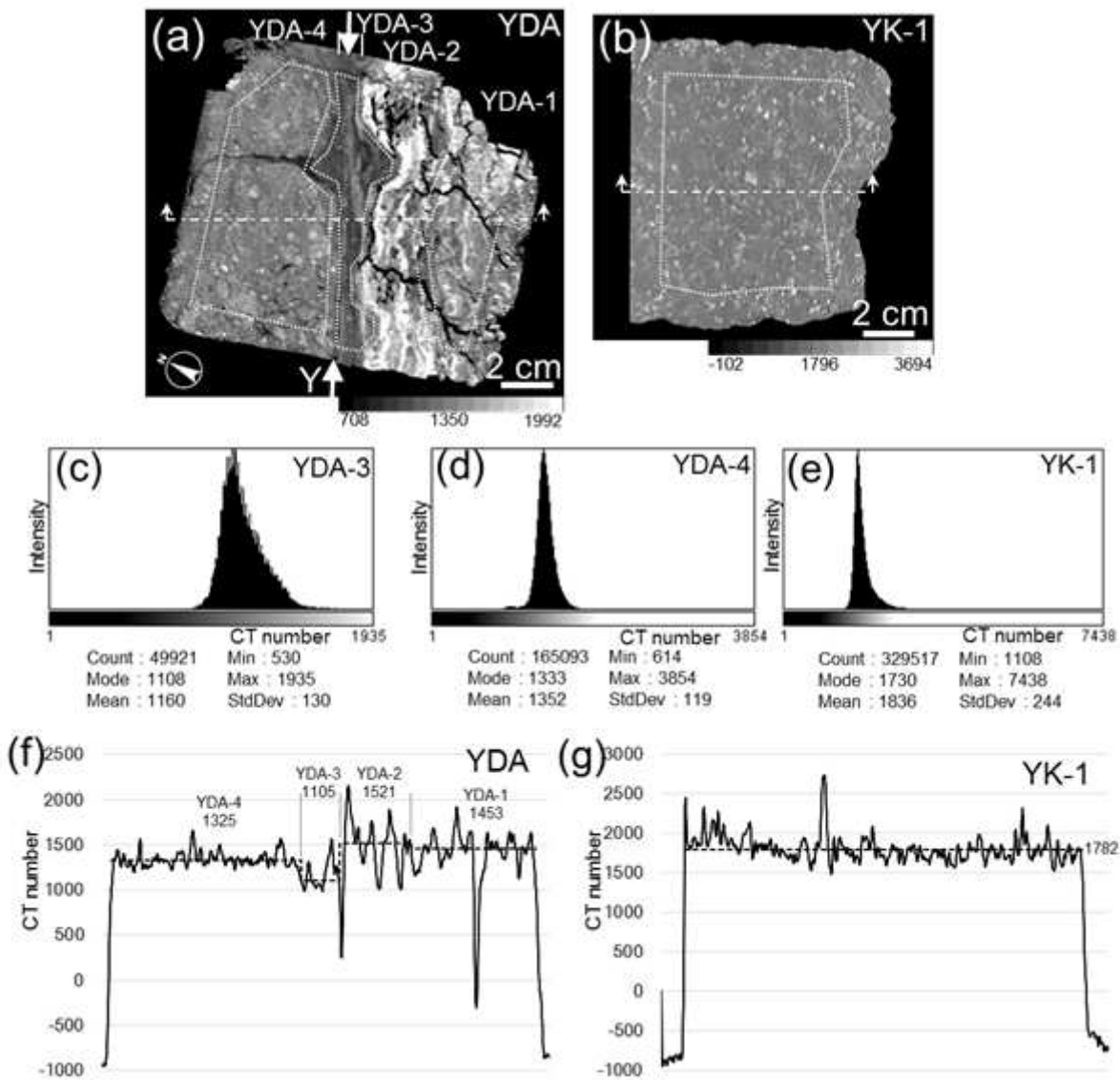


Figure 9

X-ray CT image analysis results for the Mushu outcrop samples. CT images of the (a) YDA and (b) YK-1 samples. CT number histograms for (c) YDA-3, (d) YDA-4, and (e) YK-1. The NCTM values were calculated near the center (within the white dotted lines in (a) and (b)) of each zone, with the peripheral areas excluded. CT number profiles for (f) YDA and (g) YK-1, with the values calculated along the dash-dotted lines in (a) and (b), respectively.

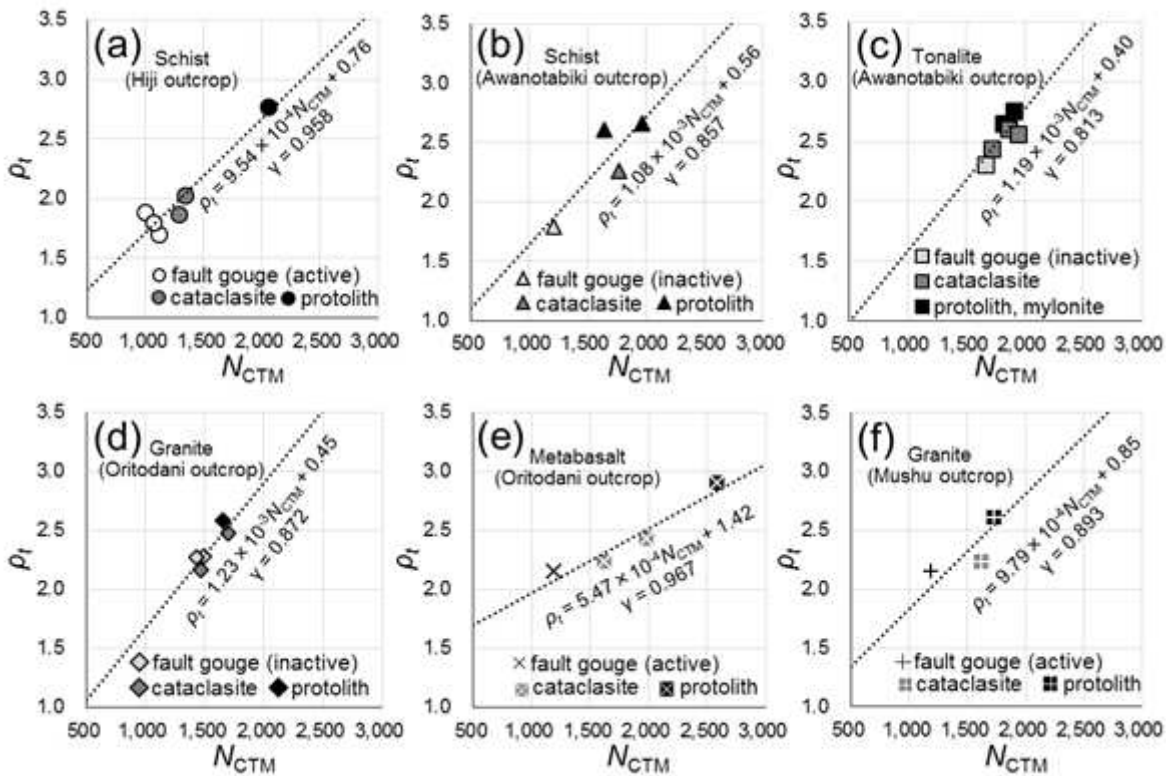


Figure 10

ρ_t – N_{CTM} crossplots for the sampled fault rocks and protoliths. (a) Schist (Hiji outcrop). (b) Schist (Awanotabiki outcrop). (c) Tonalite (Awanotabiki outcrop). (d) Granite (Oritodani outcrop). (e) Metabasalt (Oritodani outcrop). (f) Granite (Mushu outcrop).

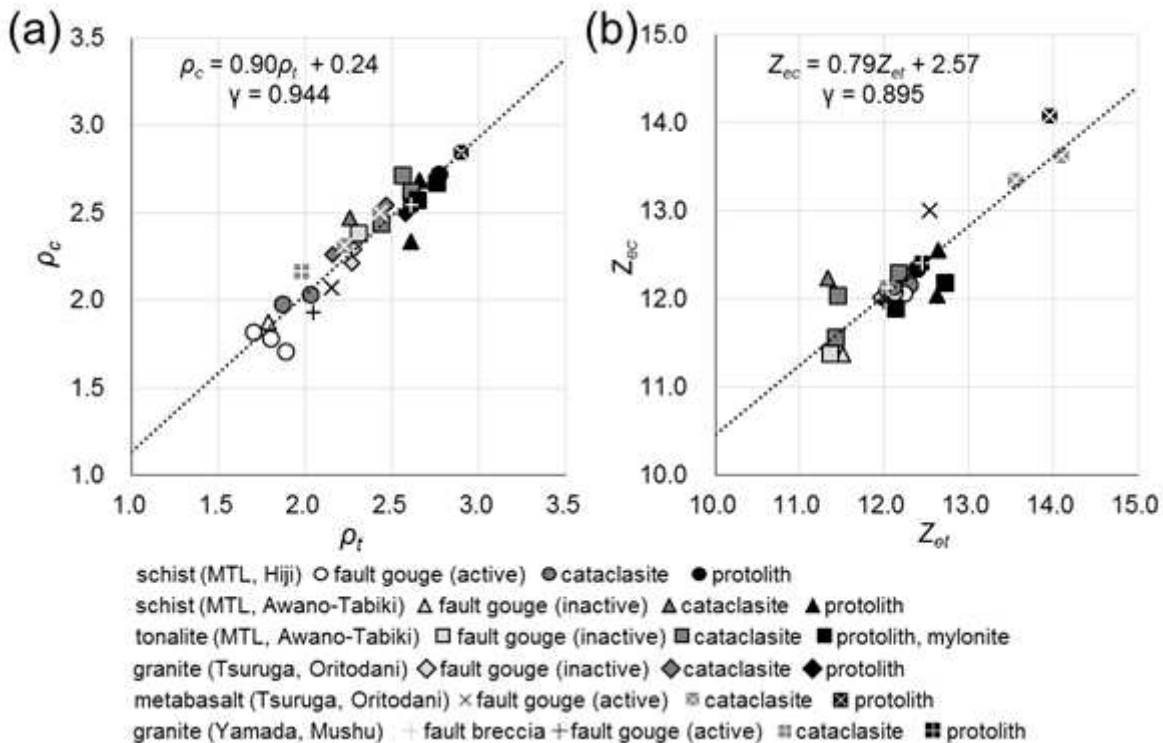


Figure 11

Crossplots of (a) the real density, ρ_t , versus the measured density, ρ_c , which is calculated from NCTM, and (b) the real effective atomic number, Z_{et} , versus the measured effective atomic number, Z_{ec} , which is calculated from NCTM. Regression lines were determined via least-squares analysis.

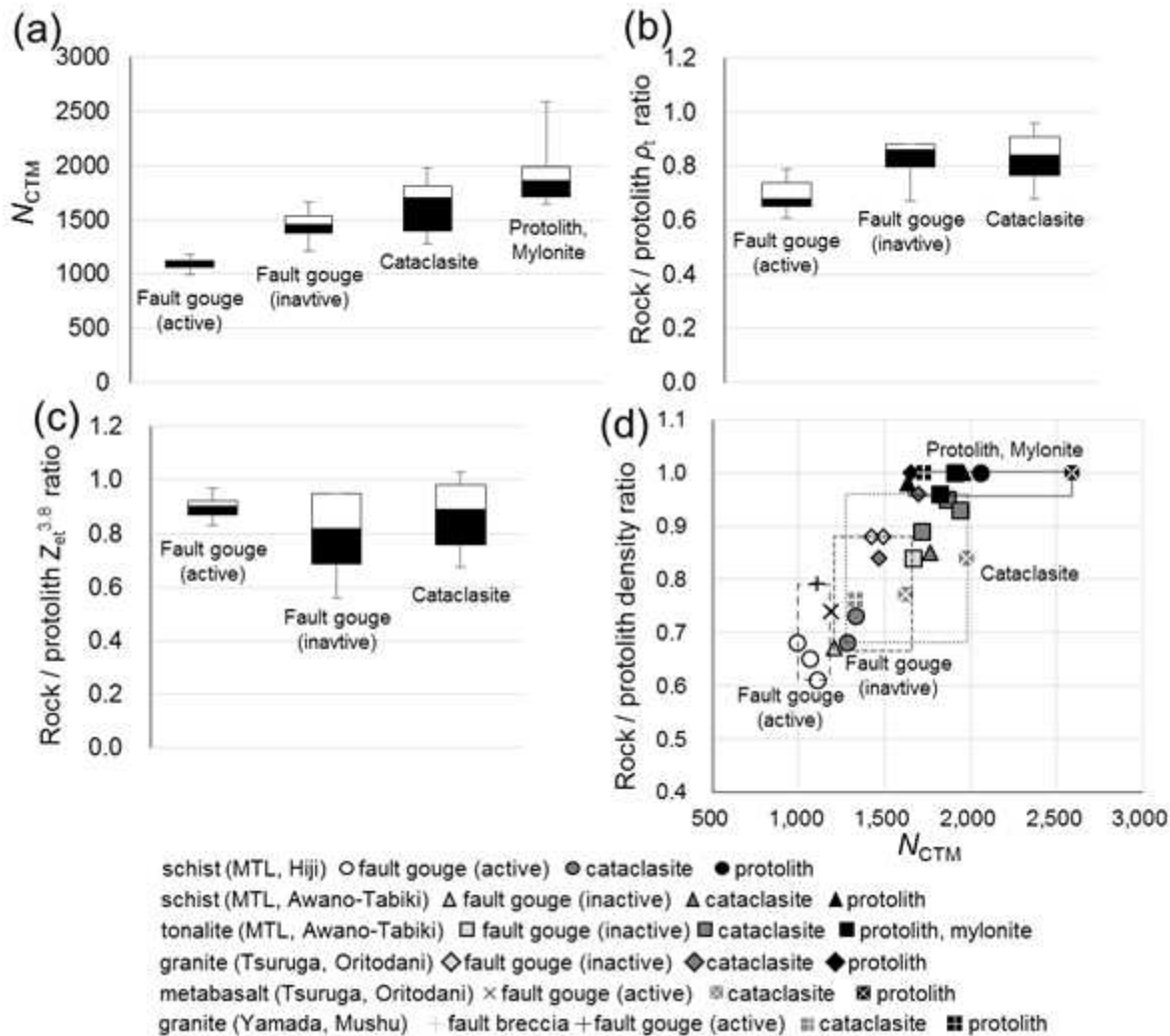


Figure 12

Box plots of (a) NCTM, (b) rock/protolith ρ_t ratio, (c) and rock/protolith $Z_{et}^{3.8}$ ratio, and (d) crossplot of NCTM versus rock/protolith ρ_t ratio.

Supplementary Files

This is a list of supplementary files associated with this preprint. Click to download.

- [Iwamori et al 2021 Graphical abstract image.png](#)
- [Iwamori et al 2021 table 1.docx](#)
- [Iwamori et al 2021 table 2.docx](#)
- [Iwamori et al 2021 table 3.docx](#)

- [Iwamori et al 2021 table 4.docx](#)
- [Iwamori et al 2021 table 5.docx](#)
- [Iwamori et al 2021 table 6.docx](#)